

ARTICLE



<https://doi.org/10.1038/s41467-022-29463-6>

OPEN

Fusion of Majorana bound states with mini-gate control in two-dimensional systems

Tong Zhou¹✉, Matthieu C. Dartialh², Kasra Sardashti², Jong E. Han¹, Alex Matos-Abiague³, Javad Shabani² & Igor Žutić¹✉

A hallmark of topological superconductivity is the non-Abelian statistics of Majorana bound states (MBS), its chargeless zero-energy emergent quasiparticles. The resulting fractionalization of a single electron, stored nonlocally as a two spatially-separated MBS, provides a powerful platform for implementing fault-tolerant topological quantum computing. However, despite intensive efforts, experimental support for MBS remains indirect and does not probe their non-Abelian statistics. Here we propose how to overcome this obstacle in mini-gate controlled planar Josephson junctions (JJs) and demonstrate non-Abelian statistics through MBS fusion, detected by charge sensing using a quantum point contact, based on dynamical simulations. The feasibility of preparing, manipulating, and fusing MBS in two-dimensional (2D) systems is supported in our experiments which demonstrate the gate control of topological transition and superconducting properties with five mini gates in InAs/Al-based JJs. While we focus on this well-established platform, where the topological superconductivity was already experimentally detected, our proposal to identify elusive non-Abelian statistics motivates also further MBS studies in other gate-controlled 2D systems.

¹ Department of Physics, University at Buffalo, State University of New York, Buffalo, NY 14260, USA. ² Center for Quantum Phenomena, Department of Physics, New York University, New York, NY 10003, USA. ³ Department of Physics and Astronomy, Wayne State University, Detroit, MI 48201, USA.
✉email: tzhou8@buffalo.edu; zigor@buffalo.edu

Proximity effects can transform common materials to acquire exotic properties¹. A striking example is a topological superconductivity hosting Majorana bound states (MBS)^{2–6}. Their non-Abelian statistics support a peculiar state of matter, where quantum information stored nonlocally is preserved under local perturbation and disorder, particularly suitable for fault-tolerant quantum computing^{7–9}. Detecting MBS is mainly focused on one-dimensional (1D) systems^{10–13} through spectral features, such as the zero-bias conductance peak (ZBCP)¹⁴. However, even stable quantized ZBCP may not correspond to MBS^{15–17}. While it is critical to identify MBS signatures that directly probe non-Abelian statistics, 1D systems require fine-tuned parameters for topological superconductivity^{4,5} and limit probing non-Abelian statistics through MBS exchange (braiding) or fusion^{7,8}.

Defects and quasiparticles in topological superconductors, or boundaries between topological and trivial regions, can bind localized Majorana zero-energy modes which behave as non-Abelian anyons^{8,9}. These zero-energy topologically-protected degenerate states, in which quantum information can be stored, are separated by the energy Δ from the excited states, as depicted in Fig. 1a. The ground states, nonlocally storing ordinary fermions, can be labeled by the fermion-parity (even or odd), reflecting 0 or 1 fermion occupancy. For an ordinary fermion, f , composed of non-overlapping Majoranas, the ground state is twofold degenerate since both fermion parities correspond to zero energy. However, bringing the two Majoranas closer removes this degeneracy, as depicted in Fig. 1b, c. The resulting multiple fusion outcomes^{8,18}

$$\gamma \times \gamma = I + \psi, \quad (1)$$

reflect the underlying non-Abelian statistics and summarize that the fusion of the two MBS behaves either as vacuum, I , or an unpaired fermion ψ , resulting in an extra charge. For the trivial fusion in Fig. 1b, when MBS with a defined parity within the same pair coalesce, the outcome is deterministic, it leads to the unchanged parity (shown to be even) with no extra charge. For the nontrivial fusion in Fig. 1c, both parities are equally likely, a probabilistic measurement would yield an extra charge. While a pioneering proposal for MBS fusion in 1D nanowires envisions gate-control realization of Fig. 1b, c¹⁹, it has important obstacles. (i) Common nanowire geometries are surrounded by superconductors, the screening makes attempted gating ineffective. (ii) Topological superconductivity requires fine-tuned parameters^{4,5}. (iii) 1D geometry complicates detecting an extra charge from fusion. (iv) Without an accurate preparation of the initial state,

the distinction between trivial and nontrivial fusion outcomes is unclear.

Here we overcome these limitations by recognizing the opportunities in 2D proximitized materials^{20–30}. We reveal how mini-gate control in planar Josephson junctions (JJs) with 2D electron gas (2DEG) provides a versatile platform to realize MBS fusion. Our 2D InAs/Al JJs have proximitized 2DEG only partially covered by superconductors. Mini-gates placed in the uncovered part strongly change the proximitized 2DEG. Unlike fine-tuned parameters for 1D nanowires, recent experiments^{31–33} reveal that in planar JJs topological superconductivity exists over a large parameter space, and is particularly robust when the phase difference, ϕ , between two superconducting regions is close to π .

By proposing a V-shaped geometry, our JJ has its apex exposed edges where the locations of the bound states, formed through fusion, simplifies the charge detection in the adjacent quantum dot (QD) using quantum point contact (QPC)^{34–36}. To distinguish the fusion outcomes in the charge detection, we reveal the importance of an accurate preparation of the initial state. We theoretically demonstrate the fundamental aspect of non-Abelian fusion that we can transform an MBS pair into an unpaired fermion while using experimental parameters for topological superconductivity from our JJs³¹. The feasibility of these findings is corroborated experimentally through the gate control of topological transition and superconducting properties and dynamical simulations of the MBS fusion.

Demonstrating fusion would be a major milestone for topological quantum computing and bridge the gap between the still controversial MBS observation³⁷ and topological quantum algorithms, largely detached from their materials implementation³⁸. While the non-Abelian signatures from MBS fusion are complementary to those obtained from braiding, experimentally the fusion is simpler. There are even schemes in topological quantum computing implemented through fusion without braiding^{39–41}.

Results

Setup and model. Building on our fabrications and experimental mini-gate control, we propose two geometries to fuse MBS, the straight and V-shaped planar Josephson junctions (SJ, VJ). Figure 2a shows the SJ setup, formed by two epitaxial superconducting layers covering a 2DEG with mini gates. A 1D normal region (N), defined between the superconducting leads $S_{1,2}$ with phases $\varphi_{1,2}$, can be tuned into the topological regime by the magnetic field B_x , the 2DEG chemical potential μ_N and the phase difference $\phi = \varphi_1 - \varphi_2$ between $S_{1,2}$, imposed by the magnetic flux Φ . For $\phi \approx \pi$, the topological superconductivity exists over a large parameter space and is particularly robust^{23,24}. With $\phi = \pi$, for a

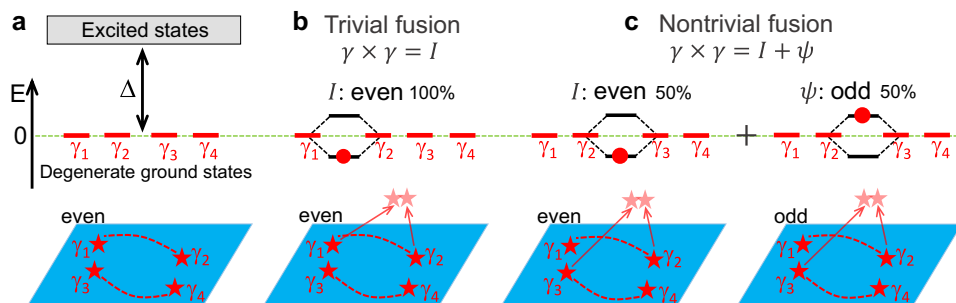


Fig. 1 Schematic of the fusion rules. **a** Topological superconductor (blue) hosting MBS, $\gamma_1, \dots, \gamma_4$. They behave as non-Abelian anyons and lead to the fourfold degeneracy in topological ground states, separated by the energy gap, Δ , from the trivial excited states. **b, c** Different fusion outcomes: trivial fusion of γ_1 and γ_2 , 100% probability to access vacuum, I (Cooper pair condensate), and nontrivial fusion of γ_2 and γ_3 , equal probabilities to access I or an unpaired fermion, ψ . Red dashed lines: paired MBS. In each case bringing closer MBS leads to the level splitting from the initial zero-energy modes. Filling the lower level, corresponding to I with even parity, means the absence of a given particle while filling the upper level refers to ψ with odd parity. We assume initially even parity of the system. The net change in the charge characterizes the nontrivial fusion.

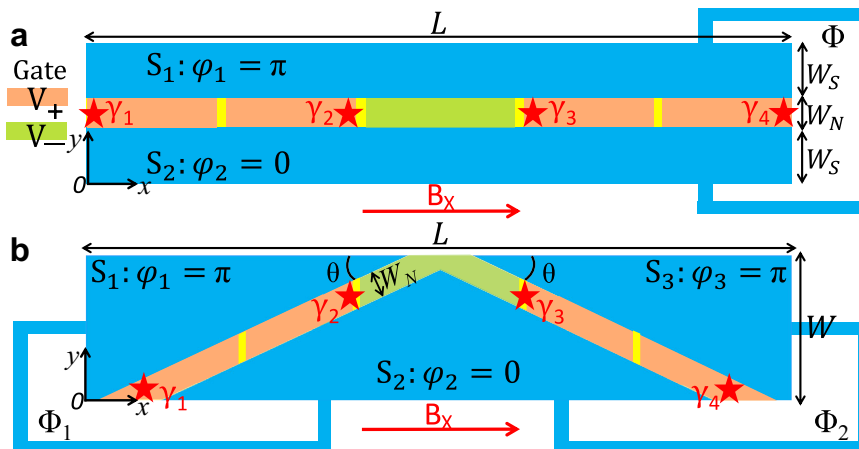


Fig. 2 Setup. **a** Straight and **b** V-shaped junction (SJ, VJ) formed by superconducting, $S_{1,2,3}$, regions (blue), partially covering a 2D electron gas (yellow). The electron density in the uncovered part is locally tuned using mini-gate voltages, $V_{1,2,3,4,5}$ (left to right). With a magnetic field B_x and superconducting phases, $\varphi_{1,2,3}$, controlled by the external fluxes Φ_1 , Φ_2 , the chemical potential of the normal region, μ_N , is locally changed to support topological (orange) and trivial (green) regions, by imposing the mini-gate voltage V_+ and V_- . MBS $\gamma_{1,2,3,4}$ (stars) form at the ends of the topological regions.

certain B_x , the topological condition can then be directly controlled by the gate voltage through the changes in μ_N ²⁴. We assume that gate voltage V_+ and V_- support topological and trivial states, respectively. With mini gates, as depicted in Fig. 2a, we expect to electrostatically create multiple topological (+) and trivial (-) regions along the N channel by imposing the corresponding voltage V_+ and V_- in the five mini gates. Multiple MBS residing at the ends of topological regions can then be moved and fused. The setup of VJ is shown in Fig. 2b. It is similar to the SJ but has a V-shaped channel with an exposed apex defined by the three superconducting leads $S_{1,2,3}$. The corresponding phases $\varphi_{1,2,3}$ can be tuned by the magnetic flux $\Phi_{1,2}$. An advantage of the VJ is that its apex provides a place to detect the fusion outcome using QPC charge sensing.

Considering the topological condition for realistic planar JJs is complicated and strongly dependent on the system parameters^{31–33}, we need to explicitly calculate the relevant V_+ and V_- . To this end, we simulate our fabricated planar JJs using the Bogoliubov-de Gennes (BdG) Hamiltonian,

$$H = \left[\frac{\mathbf{p}^2}{2m^*} - \mu_S + \mathbf{V}(x, y) + \frac{\alpha}{\hbar} (p_y \sigma_x - p_x \sigma_y) \right] \tau_z - \frac{g \mu_B}{2} \mathbf{B} \cdot \boldsymbol{\sigma} + \Delta(x, y) \tau_+ + \Delta^*(x, y) \tau_-, \quad (2)$$

where \mathbf{p} is the momentum, m^* is the effective electron mass, μ_S is the chemical potential in the considered S_i , α is the Rashba SOC strength, unless explicitly specified, $\mathbf{B} \equiv \mathbf{B}_x$. We use σ_i (τ_i) as the Pauli (Nambu) matrices in the spin (particle-hole) space and $\tau_{\pm} = (\tau_x \pm i\tau_y)/2$. $\Delta(x, y)$ is the proximity-induced superconducting pair potential, for the 2DEG below the superconducting regions, which can be expressed, using the BCS relation for the B-field suppression, as

$$\Delta(x, y) = \Delta_0 \sqrt{1 - (B/B_c)^2} e^{i\varphi_i}, \quad (3)$$

where Δ_0 is the superconducting gap at $B = 0$, B_c is the critical magnetic field, and φ_i is the corresponding S_i phase. The function $\mathbf{V}(x, y) \equiv \mu_N(x, y) - \mu_S$ describes the local changes of $\mu_N(x, y)$ in the N region due to the application of the mini-gate voltages, V_1, \dots, V_5 , as shown in Fig. 2.

In all the calculations, we choose the parameters consistent with our fabricated junctions (SJ and VJ) that also match experimental observation of robust proximity-induced superconductivity and topological states in epitaxial InAs/Al-based JJs³¹, $m^* = 0.03m_0$, where m_0 is the electron mass, and $g = 10$ for

InAs, $\Delta_0 = 0.23$ meV, $\alpha = 10$ meV nm, $B_c = 1.6$ T, and $\mu_S = 0.5$ meV. By switching V_+ and V_- through mini-gate control, we expect to generate, manipulate, and fuse MBS electrostatically. We will first demonstrate how this is realized in an SJ and then extend it to a VJ to show how the QPC charge sensing can distinguish the trivial and nontrivial fusion.

MBS fusion in an SJ. Experimental feasibility of the proposed mini-gate controlled MBS fusion builds on the demonstrated topological superconductivity in epitaxial InAs/Al planar JJs^{31,42}. This is further corroborated by using the same platform to demonstrate that mini gates can modulate the superconducting state in our fabricated SJ, shown with scanning electron microscope (SEM) images in Fig. 3a, b. With five gold mini gates covering the N region, μ_N for each region under the mini gates can be independently tuned by the bias current, I_B .

With the three inner gates depleted, the current can only flow through the two outermost regions (marked in red) as depicted in Fig. 3a. In this configuration, the device behaves as a SQUID⁴³, as seen from the map of the measured differential resistance as a function of I_B and out-of-plane magnetic field in Fig. 3c which indicates interference between the current going through the two open channels. In contrast, when the three middle gates allow current to flow, and the outermost gates are used to deplete the 2DEG in Fig. 3b, the differential resistance in Fig. 3d shows a Fraunhofer pattern, typical of a single JJ⁴³. As expected, its periodicity is close to the one of the SQUID configuration which contains the same region.

Distinct features in Fig. 3c, d show that locally μ_N is strongly changed by the mini gates, providing a clear advantage over an attempt of gate control in nanowire systems^{19,44}, where the screening by superconductors diminishes changing μ_N . Such gate-controlled superconducting response strongly supports our proposal of manipulating MBS with mini gates, when the topological superconductivity is achieved with B_x and a phase bias, ϕ . This demonstration of the mini-gate control, first established in our work, was later extended to experiments with even a larger number of mini gates⁴⁵.

Based on our fabricated device in Fig. 3, to obtain the relevant voltages V_+ (V_-) for the topological (trivial) state, we do simulations based on the geometrical parameters depicted in Fig. 2a as $L = 5$ μm , $W_S = 0.3$ μm , $W_N = 0.1$ μm , with each mini gate 1 μm long. The calculated gate-voltage-dependent energy spectrum with $B_x = 0.6$ T and $\phi = \pi$, is shown in Fig. 4a. The

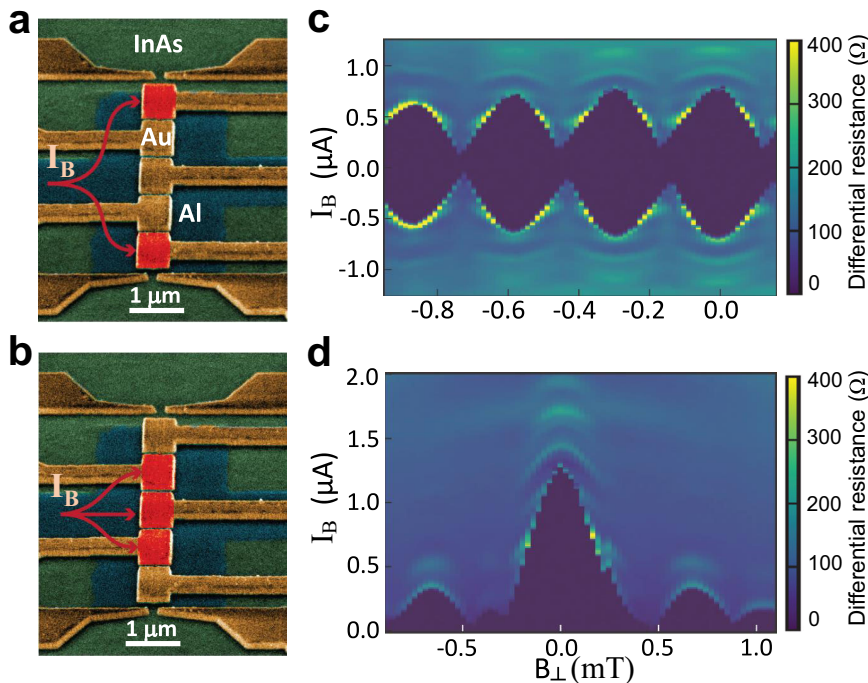


Fig. 3 Experimental mini-gate control in an SJ. **a, b** Scanning electron microscope (SEM) image of an InAs/Al SJ with five mini gates covering the normal region. Mini gates can be controlled independently and those overlaid in red indicate the regions in which the applied bias current, I_B can flow. The 2DEG is depleted under the other gates. **c, d** Differential resistance of the device as a function of the I_B and out-of-plane B_{\perp} , corresponding to the gate configuration presented in **a, b**, respectively.

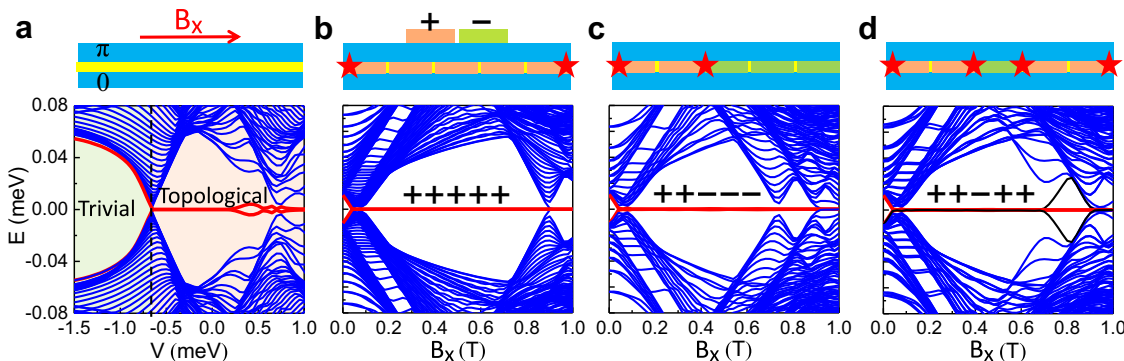


Fig. 4 Mini-gate controlled topological transitions and MBS in an SJ. **a** Schematic (top) and energy spectra (bottom) for a planar π -SJ at $B_x = 0.6$ T as a function of the gate voltage ($V = \mu_N - \mu_S$), tuned by the top gate (not shown), which covers the whole N region. The black dashed line indicates the critical gate voltage between the trivial region (green) and topological region (orange). **b-d** Schematic (top) of a planar π -SJ with MBS (stars) for + + + +, + + - -, and + + - + mini-gate configurations and the corresponding energy spectra (bottom), where $V_- = -1$ meV and $V_+ = 0$ meV are taken for - and + states, respectively. Red and black lines: evolution of finite-energy states into MBS inside the topological gap. The parameters are specified in the main text.

evolution of the lowest-energy states into zero-energy modes reveals that the MBS states emerge when the voltage exceeds the critical value $V_c = -0.7$ meV. This gives $V_+ \in (-0.7 \text{ meV}, 1 \text{ meV})$, confirmed by the spatially-localized probability density, ρ_P , and the vanishing charge density, ρ_C , while $V_- < V_c$ gives trivial states as shown in Supplementary Fig. 1. Such gate-controlled topological transition has been confirmed by the gap closing and reopening in our experiments as shown in Supplementary Fig. 2. We choose $V_+ = 0$ meV and $V_- = -1$ meV for the following simulations of mini-gate control. This identification of V_+ and V_- gives us a chance to create and manipulate multiple MBS based on different mini-gate configurations.

It is instructive to examine the topological robustness of the + + + + configuration, where all the mini gates are set at V_+ ,

which is similar to a single topological SJ without mini gates. The whole N region is expected to be topological with MBS at its ends (Fig. 4b). The calculated B_x -dependent energy spectrum shows that MBS indeed exists in a very large range of B_x , and a small $B_x \sim 0.1$ T already supports MBS, in agreement with the previous works^{23,24,46}. With mini-gate control changing + + + + into + + - -, the MBS at the right end can be moved to the left part (Fig. 4c), while breaking the topological region into two separate ones, by changing + + + + into + + - +, creates two MBS pairs (Fig. 4d). These SJ configurations are revisited in Fig. 5, where we will see that the expected control of MBS is further corroborated by the calculated ρ_P .

Following the above analysis, we propose a scenario for probing non-Abelian statistics based on fusion rules using mini-

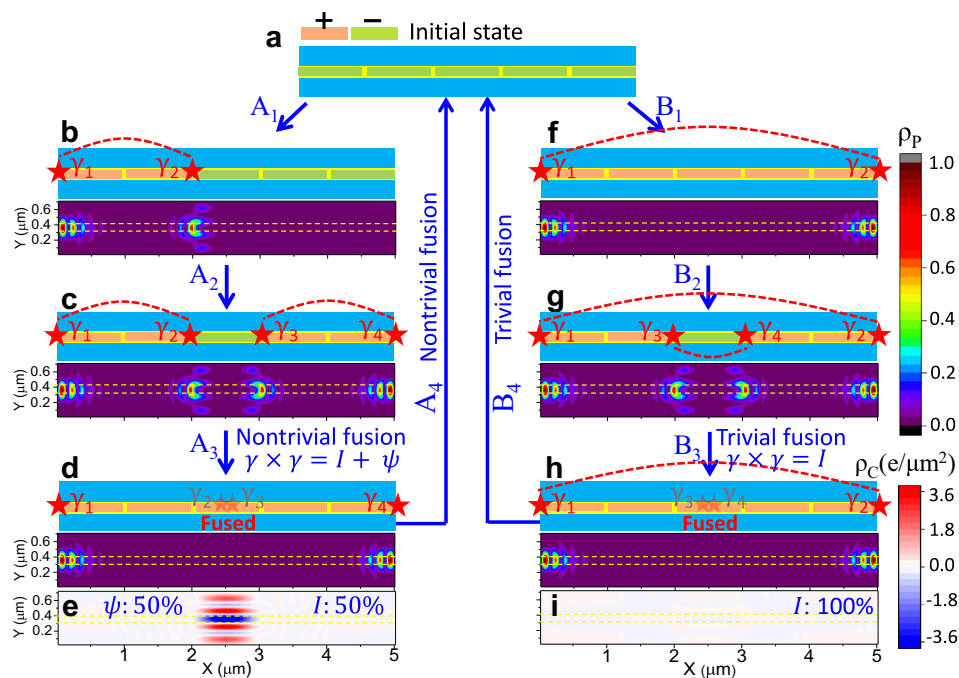


Fig. 5 Probing non-Abelian statistics through MBS fusion in an SJ. The scheme is supported by the calculated probability and charge densities, ρ_p and ρ_c . The red dashed lines link the same MBS pair, the yellow dashed lines indicate the N region covered by the mini gates. **a** Initial trivial state with —— mini gates. **b** A_1 : changing —— into +++, MBS pair (γ_1, γ_2) is created. **c** A_2 : changing +--+ into ++--, a second MBS pair (γ_3, γ_4) is created. **d** A_3 : changing +++- into +++, the MBS (γ_2, γ_3) are nontrivially fused at the center, accessing both vacuum, I , and an unpaired fermion, ψ , with 50% probability. For I , the system has no extra charge, supported by the vanishing ρ_c in **e** for the ground state after the fusion. For ψ , the system has an extra charge, supported by the finite sum of ρ_c in **e** for the ground and first excited states after the fusion. **f** B_1 : changing —— into +++, the MBS (γ_1, γ_2) are created. **g** B_2 : changing +++ into ++-, a second MBS pair (γ_3, γ_4) is created. **h** B_3 : changing ++-- into +++, the MBS (γ_3, γ_4) are trivially fused, corresponding to I with 100% probability. A_4 or B_4 : changing +++ to ——, the remaining MBS pair is fused and the system returns to the initial mini-gate configuration. MBS fusion can be repeated following such operations. ρ_p is normalized to its maximum. The (minimum and maximum) values in **e**, **i** are (-3.5, 2.9) and (-0.00009, 0.00004), respectively. All parameters are taken from Fig. 4.

gate control as shown in Fig. 5. The system is initially prepared in a trivial state (no MBS) with —— configuration. Subsequently, we can follow paths A and B to probe nontrivial and trivial fusion rules. For path A, in A_1 we first generate one MBS pair (γ_1, γ_2) by changing V_1 and V_2 from V_- to V_+ , and in A_2 the second MBS pair (γ_3, γ_4) by changing V_4 and V_5 . These two MBS pairs build two complex fermions $f_{12} = (\gamma_1 + i\gamma_2)/2$ and $f_{34} = (\gamma_3 + i\gamma_4)/2$, which can be described by the occupation numbers n_{12} and n_{34} .

Without loss of generality of demonstrating the fusion rules, we assume that the two fermion states are unoccupied, giving an initial state $|n_{12}, n_{34}\rangle = |0_{12}, 0_{34}\rangle$. To facilitate experimentally probing the fusion rules, it is important to keep the same initial states in both trivial and nontrivial fusion. We will discuss later how to prepare the initial states by adding a new operation of *initialization* before the MBS manipulations. In A_3 the change of V_3 from V_- to V_+ nontrivially fuses (γ_2, γ_3) , which accesses both the I and ψ fusion channels with equal probability. To better understand such nontrivial fusion, we reexpress the ground state in the basis of $f_{14} = (\gamma_1 + i\gamma_4)/2$ and $f_{23} = (\gamma_2 + i\gamma_3)/2$, i.e., $|0_{12}, 0_{34}\rangle = 1/\sqrt{2}(|0_{14}, 0_{23}\rangle - i|1_{14}, 1_{23}\rangle)$, where $f_{14}f_{23}|0_{14}, 0_{23}\rangle = 0$, while $|1_{14}, 1_{23}\rangle = f_{14}^\dagger f_{23}^\dagger|0_{14}, 0_{23}\rangle$. Fusing (γ_2, γ_3) induces finite energy to f_{23} , lifting the degeneracy between $|0_{14}, 0_{23}\rangle$ and $|1_{14}, 1_{23}\rangle$. As a result, measuring such a state then collapses the wavefunction with 50% probability onto either the ground state, I , or excited state with an extra quasiparticle, ψ . In A_4 fusing the remaining (γ_1, γ_4) , by changing +++ into ——,

drives the system to the initial mini-gate configuration. To verify the non-Abelian statistics, we examine a trivial fusion scheme B_1 - B_4 . Unlike in the nontrivial fusion, first (γ_1, γ_2) and then (γ_3, γ_4) are created by changing —— to +++ and then to ++-. Therefore, fusing (γ_3, γ_4) can only access the I channel with a trivial fusion because (γ_3, γ_4) belong to the same pair.

To simplify the description of MBS fusion it is helpful that the considered scheme from Fig. 5 is adiabatic, which requires that the topological gap remains open during the entire fusion. We show the corresponding evolution of the calculated low-energy spectra during the fusion in Supplementary Fig. 3. For any value of the continuously changing mini gates, the MBS are protected by the topological gap between the ground and first excited states which has the minimum value, $\Delta_{\min} \approx 6 \mu\text{eV}$. The Δ_{\min} could be enhanced by increasing the Rashba SOC or using Sn or Nb with a higher bulk Δ than in Al^{47,48}. An animation for the evolution of the energy spectrum and wavefunction probability during the nontrivial fusion process is provided in Supplementary Movie 1.

Through uncertainty relations, this Δ_{\min} imposes a lower bound for the switching time, τ , during the mini-gate operation, which can be estimated as $\tau_0 \sim \hbar/\Delta_{\min}$. In a realistic system, since the fusion involves multiple finite-size MBS pairs, their energies are not exactly zero and are characterized by their splitting, Δ_S . Therefore, the switching time should be sufficiently short to ensure the non-adiabatic transition between these nearly-degenerate MBS levels, giving an upper bound $\tau < \tau_S = \hbar/\Delta_S$. The upper bound is also constrained by the quasiparticle poisoning time, τ_p . From the previous measurements in InAs/Al systems, τ_p

was reported to be between $1\text{ }\mu\text{s}$ and 10 ms ^{49,50}. Together, $\tau_0 < \tau < \min(\tau_S, \tau_P)$ is required for adiabatic fusion. In our SJ, this constraint implies $0.1\text{ ns} < \tau < 13\text{ ns}$, which is readily realized with the existing gate-controlled employed in JJ-based qubits which are reaching GHz operation⁵¹. The feasibility of this adiabatic evolution and distinct outcomes between the nontrivial and trivial MBS fusion are important prerequisites for using the fusion rules as an experimental verification of the non-Abelian statistics. A guidance for how the fusion rules could be measured comes from the prior proposals in nanowires, suggesting using Josephson current, fermion-parity, or cavity detection^{8,11,19,52–54}.

As shown in Fig. 1, the trivial fusion deterministically gives rise to the fusion channel I , preserving the charge of the system, while in the nontrivial fusion there is a 50% probability for creating an extra charged quasiparticle ψ , which opens ways for charge detection. We expect the dynamical process of the charge creation is associated with a Cooper pair which is then quickly absorbed into the spatially-separated condensate for which the BCS formalism is adequate. Such an extra charge residing at a bound state [Supplementary Fig. 3] shows a huge local charge density difference compared to that in the I fusion channel, which is verified by the four orders of magnitude difference in the corresponding ρ_C as shown in Fig. 5e, i. When the initial states are fixed, repeating operations A_1 – A_4 from Fig. 5 is expected to give rise to charge fluctuations. In contrast, the fluctuations should be absent when repeating operations B_1 – B_4 in the nontrivial fusion process. Detecting such charge fluctuations can be a direct evidence for the MBS nontrivial fusion and non-Abelian statistics.

MBS fusion in a VJ. The previous SJ geometry provides a plausible path to MBS fusion and distinguishing the resulting outcomes. However, the corresponding charge fluctuations emerge in the interior of the central part of the N region, which is challenging to access experimentally due to the screening of superconductors and the presence of the top mini gates. Furthermore, it is unclear how to prepare the initial states, which is important to distinguish different experimental outcomes between the trivial and nontrivial fusion.

To overcome these difficulties, we propose a V-shaped geometry for the N-region where its apex is exposed to the edge, as shown in Fig. 2b. To control preparing initial states, we also add half-length mini gates (“L”, and “R”), with voltages V_L and V_R at the ends of VJ, as shown in Fig. 6a. In their topological regime, L, and R, behave as effective quantum islands, supported by our calculations [Supplementary Note 1]. With two external fluxes, Φ_1 , Φ_2 , and mini-gate control, the MBS can be fused at the apex in a similar way to that in the SJ. An advantage in the VJ is that its apex provides a place to detect the additional charge induced by MBS fusion with QPC charge sensing, successfully used in semiconducting nanostructures^{34–36} and also proposed for detection of topological superconductivity in 1D systems⁵⁴. An experimental realization of the VJ with five mini gates, fabricated using standard electron-beam lithography and InAs/Al JJs, is shown in Supplementary Fig. 5.

A key difference from the SJ is that for the VJ, B_x and the N/S interfaces are no longer aligned. To support MBS in VJs, the topological superconductivity should survive such a misalignment, characterized by the angle θ in Fig. 6a. As shown in Supplementary Fig. 4, our calculations reveal that topological superconductivity is supported for $\theta \leq 0.15\pi$. For a larger θ , the topological states become eventually fully suppressed, consistent with the trends measured in planar JJs⁵¹. Based on the misalignment angle in the geometry of the fabricated VJ from Supplementary Fig. 5, we fix $\theta = 0.1\pi$ in the following calculations.

The VJ geometry resembles half of an X-junction⁴⁶, where various MBS can be created at the ends of the N regions by phase control. Similar as discussed for an SJ, a phase difference of π between the two adjacent S regions supports topological superconductivity at a lower B_x . Therefore, as shown in Fig. 6c, we fix the phases $(\varphi_1, \varphi_2, \varphi_3)$ of S_1 , S_2 , and S_3 as $(\pi, 0, \pi)$ with external fluxes $\Phi_1 = \Phi_2 = 0.5\Phi_0$, where Φ_0 is the magnetic flux quantum, forming a π -VJ. A similar phase control with two external fluxes has been realized experimentally⁵⁵. Such a π -VJ is expected to exhibit topological superconductivity in the whole N region with MBS localized at its two ends. This can be seen in Fig. 6d when the gate voltage gives rise to topological states, analogous to the long-edge MBS in the X-junction⁴⁶.

To identify the V_+ and V_- in the π -VJ, we calculate the V -dependent energy spectrum at $B_x = 0.7\text{ T}$ (see Fig. 6c). The evolution of the lowest-energy states shows the critical $V_c = -3\text{ meV}$ in the VJ, where V smaller (larger) than V_c yields trivial (topological) states, further verified by the calculated ρ_P and ρ_C in Supplementary Fig. 6. The chosen $V_+ = 0\text{ meV}$ and $V_- = -5\text{ meV}$ are used to manipulate the MBS with various mini-gate configurations. Similar to the SJ, for the +++++ configuration, the MBS are located at the ends of the N region, supported by the calculated zero-energy modes (Fig. 6d) and ρ_P (Fig. 7c). By changing +++++ into +----, the MBS can be moved to the left side (Fig. 6e), while changing +--- into ++-- creates another MBS pair on the right side (Fig. 6f). The zero-energy bands have small oscillations in the +--- and ++-- configurations because of the limited length of the topological regions. These oscillations are suppressed by reducing the MBS overlap with an increased system size as in Supplementary Fig. 7.

Similar to the fusion protocol in Fig. 5, the MBS trivial and nontrivial fusion can be implemented in a VJ as shown in Supplementary Note 2. The spectrum evolution during the nontrivial (trivial) fusion with A_1 – A_4 (B_1 – B_4) operations is shown in Fig. 7a (Supplementary Fig. 11). We can see the two quantum island states adiabatically evolve into two MBS pairs after the operations A_{1-2}/B_{1-2} . Such two MBS pairs, marked as E and F in Fig. 7a, are localized at the ends of the topological mini gates (Fig. 7b) in the ++--++ configuration. They are chargeless before the fusion, supported by the calculated ρ_C in Fig. 7e. The operation A_3 fuses the MBS (γ_2 and γ_3) from different pairs and gives a nontrivial fusion. There is a 50% probability of attaining the ground state, G, localized at the ends of the N regions (Fig. 7c) with vanishing ρ_C (Fig. 7f), accessing the I fusion channel. The other outcome, to attain with 50% probability the excited state, H, bound at the VJ apex (Fig. 7d), is accompanied with ρ_C (Fig. 7g) more than 1000 times larger than that of the ground state at the VJ apex, accessing the ψ fusion channel. In contrast, operation B_3 trivially fuses the MBS (γ_3 and γ_4) from the same pair. The resulting outcome I is achieved with 100% probability. Therefore, the probabilistic presence or absence of an extra charge at the VJ apex is a signature of different fusion outcomes.

To experimentally realize the fusions, the switching time should be tuned to enable that the MBS are adiabatically evolved during the whole fusion process in a VJ. The required switching time of the mini-gate control could be estimated analogously as for the SJ. We obtain $0.07\text{ ns} < \tau < 7\text{ ns}$ by calculating the spectrum evolution during the whole fusion process (Fig. 7a), which is independently confirmed from our dynamical simulations shown in Supplementary Note 3.

The presence (absence) of the charge fluctuations when repeating nontrivial (trivial) is usually viewed as evidence for the MBS fusion rules. However, if each time the initial state and its occupation change randomly, the trivial fusion may also give charge fluctuations as a false signature of the fusion rules. This

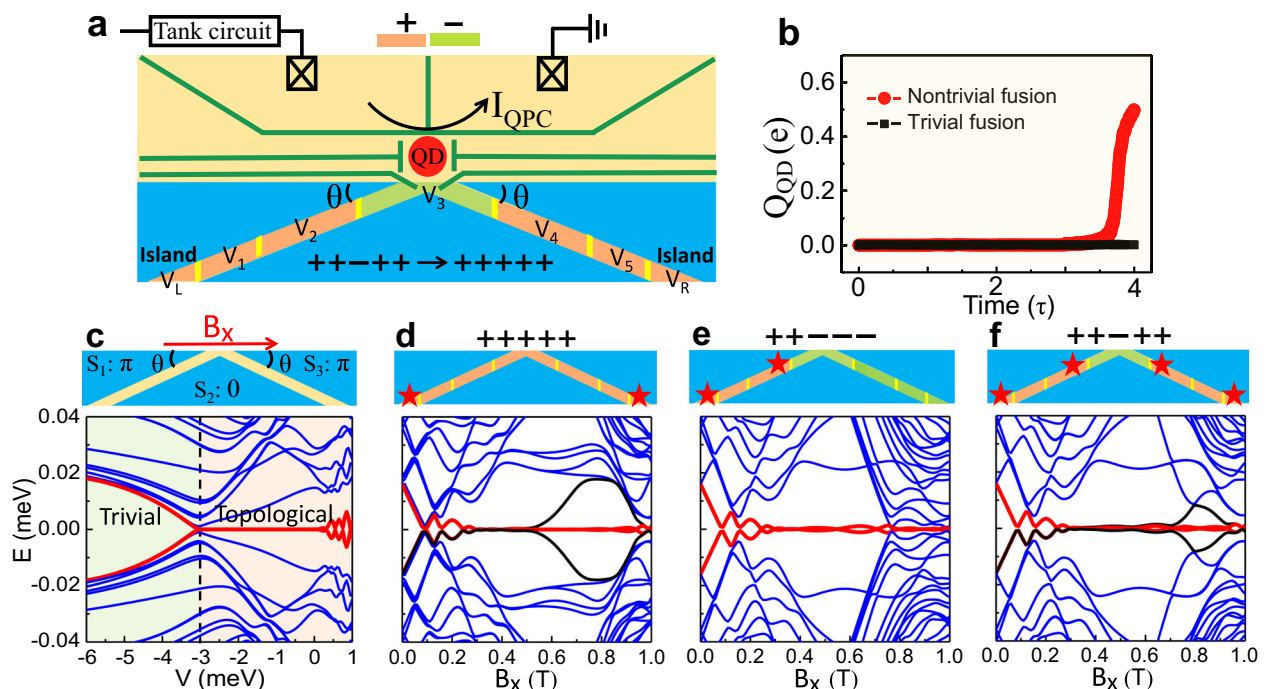


Fig. 6 Mini-gate controlled topological transition and MBS fusion in the VJ. **a** Schematic of a setup with five mini gates and two quantum islands, “L” and “R”, for the preparation of the initial states, with voltages V_{1-5} , V_L , and V_R . A quantum dot (QD) together with a quantum point contact (QPC) is coupled to the apex of the VJ to detect the fusion outcome. **b** Calculated charge average of the QD, Q_{QD} , induced from the process of the trivial and nontrivial fusion, where τ is the mini-gates switching time with $1/\tau \sim 1 \text{ GHz}$. **c** Schematic (top) and energy spectra (bottom) for a VJ with superconducting phases $(\pi, 0, \pi)$ at $B_x = 0.7 \text{ T}$ as a function of the gate voltage V , tuned by the top gate (not shown), which covers the whole N region. The black dashed line indicates the V_c between the trivial (green) and topological (orange) regions. **d-f** Schematic (top) of a VJ with MBS (stars) for the $+++++$, $+---$, and $++-+$ configurations at $B_x = 0.7 \text{ T}$ and the corresponding energy spectra (bottom). Red and black lines: evolution of finite-energy states into MBS inside the topological gap. The geometric parameters are $L = 3.6 \mu\text{m}$, $W = 0.6 \mu\text{m}$, $W_N = 0.1 \mu\text{m}$, and $\theta = 0.1\pi$. Other parameters are specified in the main text.

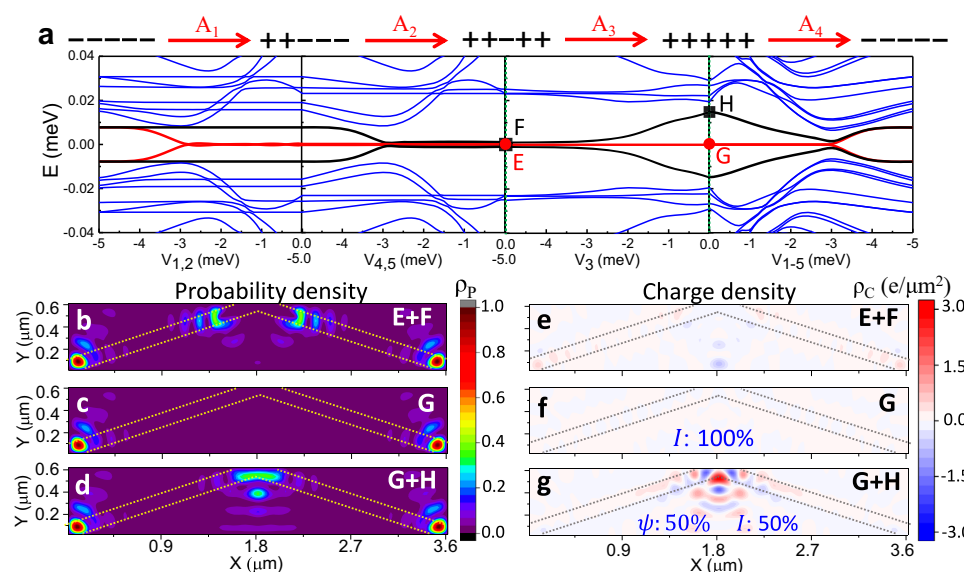


Fig. 7 Outcome of the MBS fusion in a VJ. **a** Spectrum evolution for the operations A_1 - A_4 as a function of the relevant mini-gate voltage. Red and black lines: evolution of finite-energy states into MBS inside the topological gap. E and F: the two MBS pairs (degenerate ground states) in the $++-+$ configuration (before fusion). G and H: the ground and first excited states in the $++++$ configuration (after fusion). **b-d** Sum of the probability densities, ρ_p for E and F. **e-g** The same as **b-d**, but for charge densities, ρ_C . The dashed lines mark the N regions covered by the mini gates. ρ_p is normalized to its maximum. The (minimum, maximum) values in **e-g** are $(-0.7, 0.5)$, $(-0.02, 0.03)$, and $(-1.9, 3.0)$, respectively. The parameters are taken from Fig. 6.

issue has been overlooked in previous fusion proposals^{8,19}, which neglect the effect of the initial occupations. To overcome this problem, as shown in Supplementary Note 1, we propose an initialization A_0 (B_0), further supported by our simulations, to empty the initial occupations of the quantum island and get the $|00\rangle$ state. Such initialization precedes A_1 - A_4 (B_1 - B_4) operations to realize the initial $|00\rangle$ state in every fusion cycle, which corresponds to the operations A_1 - A_3 (B_1 - B_3) for the nontrivial (trivial) fusion. Observing the presence (absence) of the charge fluctuations at the VJ apex for repeated nontrivial (trivial) fusion can then be a conclusive evidence for the fusion rules.

Readout of the fusion outcome. To detect the charge fluctuations from the fusion, we couple a QD to the VJ apex. The QD is created by confining gates³⁴, as shown in Fig. 6a, and its energy levels can be shifted by the gate voltage V_{QD} . When the energy of the lowest unoccupied state in the QD is aligned between the energy levels of the G and H states (Fig. 7a), the fusion-induced charge can transfer into the QD, giving a QD charge change, Q_{QD} . For trivial fusion, Q_{QD} is 0; while for nontrivial fusion, Q_{QD} is 0 or $1e$ with the same probability, giving an average value of $0.5e$. Such a different fusion outcome is supported by the calculated Q_{QD} , shown in Fig. 6b, by using dynamical simulations based on time-dependent BdG equation^{56,57}. More discussion and calculation details are given in Supplementary Note 3. The Q_{QD} can be detected by the attached QPC^{34–36}, because the QPC current, I_{QPC} , is very sensitive to the charge change^{35,36,54}. Such a charge sensing technique has been widely used to accurately detect the charge in QDs³⁴. After the charge sensing detection, the fusion-induced charge does not stay in the VJ. We then reset the mini-gates to the initial configuration (A_4 / B_4) and do the initialization to make sure that each fusion cycle has the same initial state.

By repeating the operations of A_0 - A_4 (B_0 - B_4), we can repeat the MBS fusion with the same occupation state $|00\rangle$ as shown in the fusion protocols (Supplementary Note 2). Every time the fusion occurs (the system goes into $++++$ after A_3 / B_3), we use QPC charge sensing to detect Q_{QD} . The detected current, I_{QPC} , through the QPC is denoted by I_{TF} (I_{NF}) for the trivial (nontrivial) fusion. While the expected I_{TF} remains the same, the I_{NF} fluctuates during the fusion cycles. To suppress the possible trivial background charge fluctuation, we can focus on the difference, Δ_{IF} , between the I_{TF} and I_{NF} . Measuring such a fluctuating Δ_{IF} is a direct conclusive evidence for the non-Abelian statistics of MBS.

Discussion

While using the V-shaped junction requires some care in its design, such that the magnitude of the misalignment angle between the N/S interface and the applied in-plane magnetic field is not too large^{31,46}, there are also important advantages of employing similar non-collinear structures to more completely manipulate MBS in 2D platforms and overcome the geometrical constraints of 1D systems. Within the same device footprint, it is possible to pattern non-collinear structures where MBS are further separated and their hybridization is reduced to better attain the limit of chargeless zero-energy states. These 2D opportunities allow using zigzag structures for improved robustness of MBS⁵⁸ or creating multiple MBS⁴⁶. Progress in fabricating superconducting structures with topological insulators^{55,59} expands materials candidates to implement non-collinear JJs as platforms for MBS.

In the present work, we have considered using the external flux control which can be conventionally realized through an out-of-plane applied magnetic field. We have theoretically demonstrated the fundamental aspect of non-Abelian fusion that we can

transform an MBS pair into an unpaired fermion while using experimental parameters for topological superconductivity³¹. Our experiments on mini-gate controlled superconducting properties in JJ and dynamical simulations of the MBS fusion are reassuring for the feasibility of these findings. However, future efforts may also take advantage of tunable magnetic textures as a method to implement a highly-localized flux control. Such textures could be implemented with an array of magnetic elements or magnetic multilayers^{21,22,27,60–64}, as well as by using magnetic skyrmions^{65–68}. The presence of magnetic textures also extends the control of the spin-orbit coupling (SOC), beyond the usual classification into Rashba or Dresselhaus contribution²⁵, as such textures generate synthetic SOC^{21,22,69}, and allow supporting MBS even in systems with inherently small SOC^{52,62}.

Methods

Simulations. The calculated results are obtained by numerically solving the BdG Hamiltonian from Eq. (2), using the Kwant package⁷⁰. The dynamical simulations are performed by solving the time-dependent BdG equations^{56,57}, as given in Supplementary Note 3.

Fabrications. The JJ structure is grown on a semi-insulating InP (100) substrate, followed by a graded buffer layer. The quantum well consists of a 4 nm layer of InAs grown on a 6 nm layer of $\text{In}_{0.81}\text{Ga}_{0.19}\text{As}$. The InAs layer is capped by a 10 nm $\text{In}_{0.81}\text{Ga}_{0.19}\text{As}$ layer to produce an optimal interface while maintaining high 2DEG mobility, followed by in situ growth of epitaxial Al (111). JJs are fabricated on the same wafer exhibit a highly-transparent interface between the superconducting layer and the 2DEG. The fabrication process consists of three steps of electron-beam (e-beam) lithography using PMMA resist. After the first lithography, the deep semiconductor mesas are etched using first Transene type D to etch the Al and then an III-V wet etch [$\text{C}_6\text{H}_8\text{O}_7(1\text{M})\text{:H}_3\text{PO}_4(85\% \text{ in mass})\text{:H}_2\text{O}_2(30\% \text{ in mass})\text{:H}_2\text{O} = 18.3\text{:0.43}\text{:1.73.3}$]. The second lithography is used to define the JJ gap which is etched using Transene type D. A layer of 90 nm of SiO_x was then deposited using e-beam evaporation and finally, the gates were patterned using e-beam lithography followed by e-beam evaporation of 5 nm of Ti followed by 45 nm of Au.

Measurements. The device has been measured in an Oxford Triton dilution refrigerator fitted with a 6.3–1.5 T vector magnet which has a base temperature of 7 mK. All transport measurements are performed using standard dc and lock-in techniques at low frequencies and excitation current $I_{\text{ac}} = 10 \text{ nA}$.

Data availability

The data that support the findings of this study are available within the paper and its Supplementary Information. Additional data are available from the corresponding authors upon reasonable request.

Code availability

The computation code information for getting the theoretical results is available from the corresponding authors upon reasonable request.

Received: 21 April 2021; Accepted: 16 March 2022;

Published online: 01 April 2022

References

- Žutić, I., Matos-Abiague, A., Scharf, B., Dery, H. & Belashchenko, K. Proximity-induced materials. *Mater. Today* **22**, 85–107 (2019).
- Kitaev, A. Y. Unpaired Majorana fermions in quantum wires. *Phys.-Usp.* **44**, 131 (2001).
- Fu, L. & Kane, C. L. Superconducting proximity effect and Majorana fermions at the surface of a topological insulator. *Phys. Rev. Lett.* **100**, 096407 (2008).
- Lutchyn, R. M., Sau, J. D. & Das Sarma, S. Majorana fermions and a topological phase transition in semiconductor-superconductor heterostructures. *Phys. Rev. Lett.* **105**, 077001 (2010).
- Oreg, Y., Refael, G. & von Oppen, F. Helical liquids and Majorana bound states in quantum wires. *Phys. Rev. Lett.* **105**, 177002 (2010).
- Klinovaja, J., Stano, P. & Loss, D. Transition from fractional to Majorana fermions in Rashba nanowires. *Phys. Rev. Lett.* **109**, 236801 (2012).
- Nayak, C., Simon, S. H., Stern, A., Freedman, M. & Das Sarma, S. Non-Abelian anyons and topological quantum computation. *Rev. Mod. Phys.* **80**, 1083–1159 (2008).

8. Aasen, D. et al. Milestones toward Majorana-based quantum computing. *Phys. Rev. X* **6**, 031016 (2016).
9. Das Sarma, S., Freedman, M. & Nayak, C. Majorana zero modes and topological quantum computation. *NPJ Quantum Inf.* **1**, 150001 (2015).
10. Mourik, V. et al. Signatures of Majorana fermions in hybrid superconductor-semiconductor nanowire devices. *Science* **336**, 1003 (2012).
11. Rokhinson, L. P., Liu, X. & Furdyna, J. K. The fractional a.c. Josephson effect in a semiconductor-superconductor nanowire as a signature of Majorana particles. *Nat. Phys.* **8**, 795–799 (2012).
12. Deng, M. T. et al. Anomalous zero-bias conductance peak in a Nb-InSb nanowire-Nb hybrid device. *Nano Lett.* **12**, 6414–6419 (2012).
13. Nadj-Perge, S. et al. Observation of Majorana fermions in ferromagnetic atomic chains on a superconductor. *Science* **346**, 602–607 (2014).
14. Sengupta, K., Žutić, I., Kwon, H.-J., Yakovenko, V. M. & Das Sarma, S. Midgap edge states and pairing symmetry of quasi-one-dimensional organic superconductors. *Phys. Rev. B* **63**, 144531 (2001).
15. Zhang, H. et al. Large zero-bias peaks in InSb-Al hybrid semiconductor-superconductor nanowire devices. Preprint at [arXiv:2101.11456](https://arxiv.org/abs/2101.11456) (2021).
16. Yu, P. et al. Non-Majorana states yield nearly quantized conductance in proximitized nanowires. *Nat. Phys.* **17**, 482–488 (2021).
17. Pan, H., Cole, W. S., Sau, J. D. & Das Sarma, S. Generic quantized zero-bias conductance peaks in superconductor-semiconductor hybrid structures. *Phys. Rev. B* **101**, 024506 (2020).
18. Lahtinen, V. T. & Pachos, J. K. A short introduction to topological quantum computation. *SciPost Phys.* **3**, 021 (2017).
19. Alicea, J., Oreg, Y., Refael, G., von Oppen, F. & Fisher, M. P. A. Non-Abelian statistics and topological quantum information processing in 1D wire networks. *Nat. Phys.* **7**, 412–417 (2011).
20. Shabani, J. et al. Two-dimensional epitaxial superconductor-semiconductor heterostructures: a platform for topological superconducting networks. *Phys. Rev. B* **93**, 155402 (2016).
21. Fatin, G. L., Matos-Abiague, A., Scharf, B. & Žutić, I. Wireless Majorana bound states: from magnetic tunability to braiding. *Phys. Rev. Lett.* **117**, 077002 (2016).
22. Matos-Abiague, A. et al. Tunable magnetic textures: from Majorana bound states to braiding. *Solid State Commun.* **262**, 1–6 (2017).
23. Pientka, F. et al. Topological superconductivity in a planar Josephson junction. *Phys. Rev. X* **7**, 021032 (2017).
24. Hell, M., Leijnse, M. & Flensberg, K. Two-dimensional platform for networks of Majorana bound states. *Phys. Rev. Lett.* **118**, 107701 (2017).
25. Scharf, B., Pientka, F., Ren, H., Yacoby, A. & Hankiewicz, E. M. Tuning topological superconductivity in phase-controlled Josephson junctions with Rashba and Dresselhaus spin-orbit coupling. *Phys. Rev. B* **99**, 214503 (2019).
26. Liu, J., Wu, Y., Sun, Q.-F. & Xie, X. C. Flux-induced topological superconductor in planar Josephson junction. *Phys. Rev. B* **100**, 235131 (2019).
27. Zhou, T., Mohanta, N., Han, J. E., Matos-Abiague, A. & Žutić, I. Tunable magnetic textures in spin valves: from spintronics to Majorana bound states. *Phys. Rev. B* **99**, 134505 (2019).
28. Setiawan, F., Wu, C.-T. & Levin, K. Full proximity treatment of topological superconductors in Josephson-junction architectures. *Phys. Rev. B* **99**, 174511 (2019).
29. Hegde, S. S. et al. A topological Josephson junction platform for creating, manipulating, and braiding Majorana bound states. *Ann. Phys.* **423**, 168326 (2020).
30. Alidoust, M., Shen, C. & Žutić, I. Cubic spin-orbit coupling and anomalous Josephson effect in 2D planar junctions. *Phys. Rev. B* **103**, L060503 (2021).
31. Dartailh, M. C. et al. Phase signature of topological transition in Josephson junctions. *Phys. Rev. Lett.* **126**, 036802 (2021).
32. Fornieri, A. et al. Evidence of topological superconductivity in planar Josephson junctions. *Nature* **569**, 89–92 (2019).
33. Ren, H. et al. Topological superconductivity in a phase-controlled Josephson junction. *Nature* **569**, 93–98 (2019).
34. Hanson, R., Kouwenhoven, L. P., Petta, J. R., Tarucha, S. & Vandersypen, L. M. K. Spins in few-electron quantum dots. *Rev. Mod. Phys.* **79**, 1217–1265 (2007).
35. Barthel, C., Reilly, D. J., Marcus, C. M., Hanson, M. P. & Gossard, A. C. Rapid single-shot measurement of a singlet-triplet qubit. *Phys. Rev. Lett.* **103**, 160503 (2009).
36. Reilly, D. J., Marcus, C. M., Hanson, M. P. & Gossard, A. C. Fast single-charge sensing with a rf quantum point contact. *Appl. Phys. Lett.* **91**, 162101 (2007).
37. Aguado, R. & Kouwenhoven, L. P. Majorana qubits for topological quantum computing. *Phys. Today* **73**, 6, 44–50 (2020).
38. Brown, B. J., Laubscher, K., Kesselring, M. S. & Wootton, J. R. Poking holes and cutting corners to achieve Clifford gates with the surface code. *Phys. Rev. X* **7**, 021029 (2017).
39. Bonderson, P., Freedman, M. & Nayak, C. Measurement-only topological quantum computation via anyonic interferometry. *Ann. Phys.* **324**, 787–826 (2009).
40. Litinski, D. & von Oppen, F. Braiding by Majorana tracking and long-range CNOT gates with color codes. *Phys. Rev. B* **96**, 205413 (2017).
41. Beenakker, C. W. J. Search for non-Abelian Majorana braiding statistics in superconductors. *SciPost Phys. Lect. Notes* **15**, 1–29 (2020).
42. Barati, F. et al. Tuning supercurrent in Josephson field-effect transistors using h-BN dielectric. *Nano Lett.* **21**, 1915–1920 (2021).
43. Tinkham, M. *Introduction to Superconductivity* (McGraw-Hill, 1996).
44. Bauer, B., Karzig, T., Mishmash, R. V., Antipov, A. E. & Alicea, J. Dynamics of Majorana-based qubits operated with an array of tunable gates. *SciPost Phys.* **5**, 004 (2018).
45. Elfeky, B. H. et al. Local control of supercurrent density in epitaxial planar Josephson junctions. *Nano Lett.* **21**, 8274–8280 (2021).
46. Zhou, T. et al. Phase control of Majorana bound states in a topological X junction. *Phys. Rev. Lett.* **124**, 137001 (2020).
47. Sau, J. D., Tewari, S., Lutchyn, R. M., Stanescu, T. D. & Das Sarma, S. Non-Abelian quantum order in spin-orbit-coupled semiconductors: search for topological Majorana particles in solid-state systems. *Phys. Rev. B* **82**, 214509 (2010).
48. Pakizer, J. D., Scharf, B. & Matos-Abiague, A. Crystalline anisotropic topological superconductivity in planar Josephson junctions. *Phys. Rev. Res.* **3**, 013198 (2021).
49. Albrecht, S. M. et al. Transport signatures of quasiparticle poisoning in a Majorana island. *Phys. Rev. Lett.* **118**, 137701 (2017).
50. Higginbotham, A. P. et al. Parity lifetime of bound states in a proximitized semiconductor nanowire. *Nat. Phys.* **11**, 1017–1021 (2015).
51. Krantz, P. et al. A quantum engineer’s guide to superconducting qubits. *Appl. Phys. Rev.* **6**, 021318 (2019).
52. Desjardins, M. M. et al. Synthetic spin-orbit interaction for Majorana devices. *Nat. Mater.* **18**, 1060–1064 (2019).
53. Ben-Shach, G. et al. Detecting Majorana modes in one-dimensional wires by charge sensing. *Phys. Rev. B* **91**, 045403 (2015).
54. Wimmer, M., Akhmerov, A. R., Dahlhaus, J. P. & Beenakker, C. W. J. Quantum point contact as a probe of a topological superconductor. *New. J. Phys.* **13**, 053016 (2011).
55. Yang, G. et al. Protected gap closing in Josephson trijunctions constructed on Bi₂Te₃. *Phys. Rev. B* **100**, 180501(R) (2019).
56. Amorim, C. S., Ebihara, K., Yamakage, A., Tanaka, Y. & Sato, M. Majorana braiding dynamics in nanowires. *Phys. Rev. B* **91**, 174305 (2015).
57. Sanno, T., Miyazaki, S., Mizushima, T. & Fujimoto, S. Ab initio simulation of non-Abelian braiding statistics in topological superconductors. *Phys. Rev. B* **103**, 054504 (2021).
58. Laeven, T., Nijholt, B., Wimmer, M. & Akhmerov, A. R. Enhanced proximity effect in zigzag-shaped Majorana Josephson junctions. *Phys. Rev. Lett.* **125**, 086802 (2020).
59. Schüffelen, P. et al. Selective area growth and stencil lithography for in situ fabricated quantum devices. *Nat. Nanotechnol.* **14**, 825–831 (2019).
60. Mohanta, N. et al. Electrical control of Majorana bound states using magnetic stripes. *Phys. Rev. Appl.* **12**, 034048 (2019).
61. Palacio-Morales, A. et al. Atomic-scale interface engineering of Majorana edge modes in a 2D magnet-superconductor hybrid system. *Sci. Adv.* **5**, eaav6600 (2019).
62. Turcotte, S., Boutin, S., Camirand Lemyre, J., Garate, I. & Pioro-Ladrière, M. Optimized micromagnet geometries for Majorana zero modes in low g-factor materials. *Phys. Rev. B* **102**, 125425 (2020).
63. Ronetti, F., Plekhanov, K., Loss, D. & Klinovaja, J. Magnetically confined bound states in Rashba systems. *Phys. Rev. Res.* **2**, 022052(R) (2020).
64. Wei, P., Manna, S., Eich, M., Lee, P. & Moodera, J. Superconductivity in the surface state of noble metal gold and its Fermi level tuning by EuS dielectric. *Phys. Rev. Lett.* **122**, 247002 (2019).
65. Yang, G., Stano, P., Klinovaja, J. & Loss, D. Majorana bound states in magnetic skyrmions. *Phys. Rev. B* **93**, 224505 (2016).
66. Güngördü, U., Sandhoefner, S. & Kovalev, A. A. Stabilization and control of Majorana bound states with elongated skyrmions. *Phys. Rev. B* **97**, 115136 (2018).
67. Garnier, M., Mesaros, A. & Simon, P. Topological superconductivity with deformable magnetic skyrmions. *Commun. Phys.* **2**, 126 (2019).
68. Mascot, E., Bedow, J., Graham, M., Rachel, S. & Morr, D. K. Topological superconductivity in skyrmion lattices. *npj Quantum Mater.* **6**, 1–6 (2021).
69. Kjaergaard, M., Wölms, K. & Flensberg, K. Majorana fermions in superconducting nanowires without spin-orbit coupling. *Phys. Rev. B* **85**, 020503(R) (2012).
70. Groth, C. W., Wimmer, M., Akhmerov, A. R. & Waantal, X. Kwant: a software package for quantum transport. *New J. Phys.* **16**, 063065 (2014).

Acknowledgements

We thank Jie Liu for the helpful discussion. This work is supported by US ONR Grant No. N000141712793 (I.Ž., J.H., and A.M.-A.), DARPA Grant No. DP18AP90007, and the University at Buffalo Center for Computational Research.

Author contributions

T.Z. and I.Ž. conceived the study. T.Z. performed the calculations and analysis with J.H., A.M.-A., and I.Ž. providing input. M.C.D., K.S., and J.S. fabricated the samples and performed the experimental measurements and analysis. T.Z. and I.Ž. wrote the paper. All authors were involved in the discussion and editing of the paper.

Competing interests

The authors declare no competing interests.

Additional information

Supplementary information The online version contains supplementary material available at <https://doi.org/10.1038/s41467-022-29463-6>.

Correspondence and requests for materials should be addressed to Tong Zhou Igor Žutić.

Peer review information *Nature Communications* thanks the anonymous reviewer(s) for their contribution to the peer review of this work.

Reprints and permission information is available at <http://www.nature.com/reprints>

Publisher's note Springer Nature remains neutral with regard to jurisdictional claims in published maps and institutional affiliations.



Open Access This article is licensed under a Creative Commons Attribution 4.0 International License, which permits use, sharing, adaptation, distribution and reproduction in any medium or format, as long as you give appropriate credit to the original author(s) and the source, provide a link to the Creative Commons license, and indicate if changes were made. The images or other third party material in this article are included in the article's Creative Commons license, unless indicated otherwise in a credit line to the material. If material is not included in the article's Creative Commons license and your intended use is not permitted by statutory regulation or exceeds the permitted use, you will need to obtain permission directly from the copyright holder. To view a copy of this license, visit <http://creativecommons.org/licenses/by/4.0/>.

© The Author(s) 2022

Supplementary Information

Fusion of Majorana bound states with mini-gate control in two-dimensional systems

Tong Zhou,^{1,*} Matthieu C. Dartailh,² Kasra Sardashti,² Jong E. Han,¹
Alex Matos-Abiague,³ Javad Shabani,² and Igor Žutić^{1,†}

¹Department of Physics, University at Buffalo, State University of New York, Buffalo, NY 14260, USA

²Center for Quantum Phenomena, Department of Physics, New York University, NY 10003, USA

³Department of Physics and Astronomy, Wayne State University, Detroit, MI 48201, USA

Corresponding author emails: tzhou8@buffalo.edu; zigor@buffalo.edu

This file includes:

Supplementary Figures:

Supplementary Fig. 1: Calculated gate-controlled topological transition in an SJ.

Supplementary Fig. 2: Experimental gate-controlled topological transition in an SJ.

Supplementary Fig. 3: Spectrum evolution during the MBS fusion in an SJ.

Supplementary Fig. 4: MBS robustness against the deviation of the magnetic field from the junction interface.

Supplementary Fig. 5: SEM image for the fabricated VJ with 5 mini-gates.

Supplementary Fig. 6: Gate-controlled topological transition in a VJ.

Supplementary Fig. 7: Energy spectrum and charge densities for a VJ with a larger size.

Supplementary Notes:

Supplementary Note 1: Preparation of the initial states through initializations.

Supplementary Note 2: Protocol and spectrum evolution for the MBS fusion in a VJ.

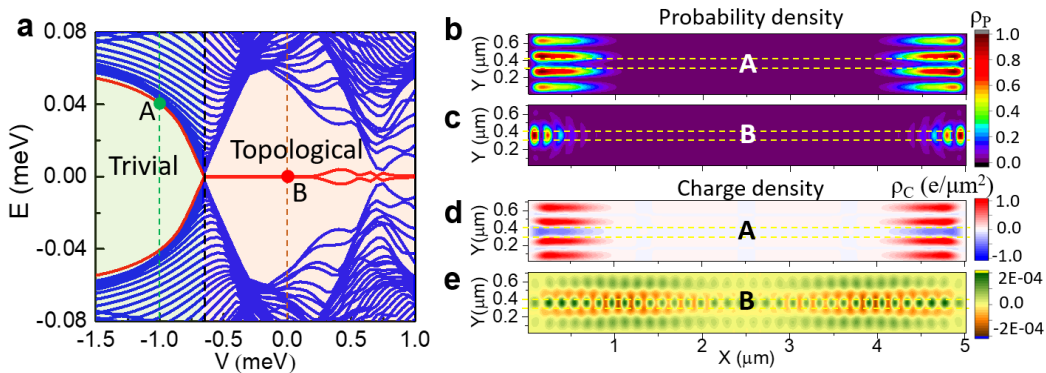
Supplementary Note 3: Dynamical simulations for the MBS fusion in a VJ.

Supplementary Movies:

Supplementary Movie 1. An animation for the evolutions of the energy spectrum and wavefunction probabilities of the Majorana bound states during the nontrivial fusion in the straight Josephson junction with mini-gate control.

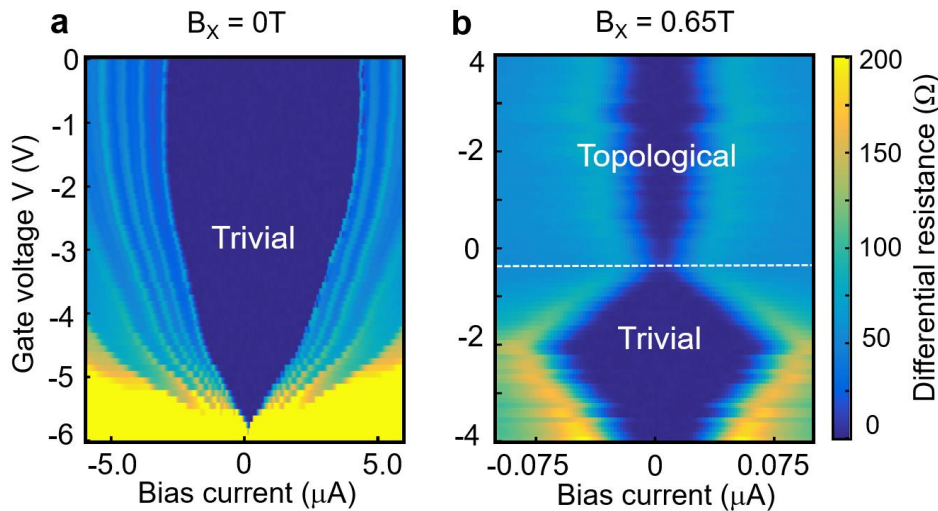
Supplementary Fig. 1: Calculated gate-controlled topological transition in an SJ

Supplementary Fig. 1 provides a gate-controlled evolution of the energy spectra, the probability density, ρ_P , and charge density, ρ_C , for the trivial and topological states in the SJ. Here, ρ_P and ρ_C are given by $\rho_P = |u|^2 + |v|^2$, and $\rho_C = e(|u|^2 - |v|^2)$, where e is the charge of the electron, while u and v are the particle and hole components of the wavefunction, respectively [1, 2]. For topological states, which are Majorana bound states (MBS), the wavefunctions are localized at the ends of the normal (N) region and the charge densities are vanishingly small and spread along the whole normal region. For the trivial states, the wavefunctions are more delocalized, while the charge densities are much larger. These results are in agreement with the previous work [3, 4], showing different properties of the trivial states and topological states.



Supplementary Fig. 1. **a** The same as Fig. 4a in the main text, but with A (B) marking the lowest-energy states at $V = -1$ (0) meV in the trivial (topological) region. **b** and **c** Probability density, ρ_P , normalized to its maximum value, for the lowest-energy states (red lines) at $V = -1.0$ meV (marked as A) in the trivial region and $V = 0$ meV (marked as B) in the topological region, respectively. **d** and **e** The same as **b** and **c**, but for charge density, ρ_C . The parameters are taken from Fig. 4 in the main text.

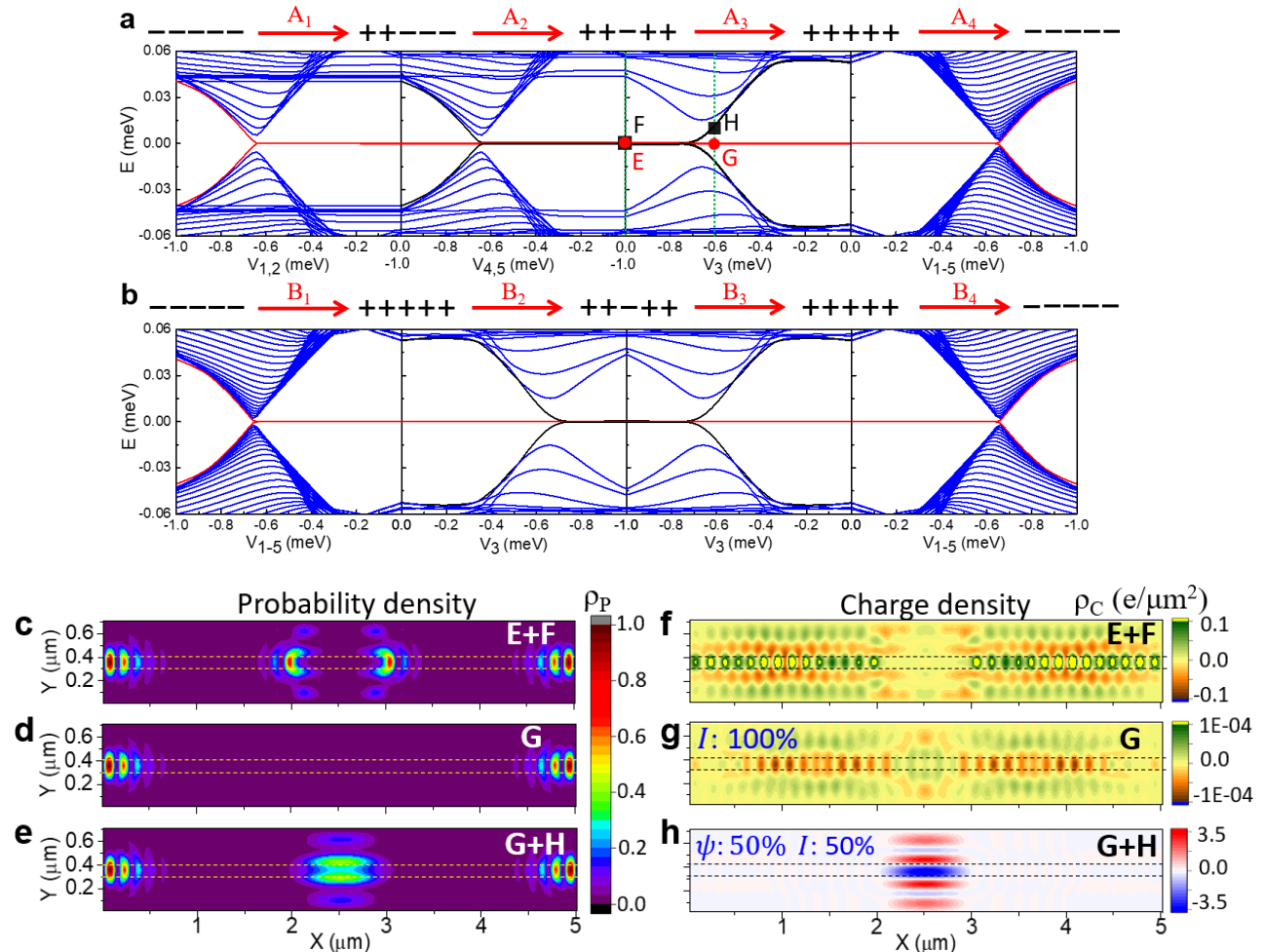
Supplementary Fig. 2: Experimental gate-controlled topological transition in an SJ



Supplementary Fig. 2. **a** Measured differential resistance for the SJ as a function of the applied gate voltage (V) with $B_x = 0$ T and **b** $B_x = 0.65$ T, consistent with the gap closing and reopening.

Supplementary Fig. 3: Spectrum evolution during the MBS fusion in an SJ

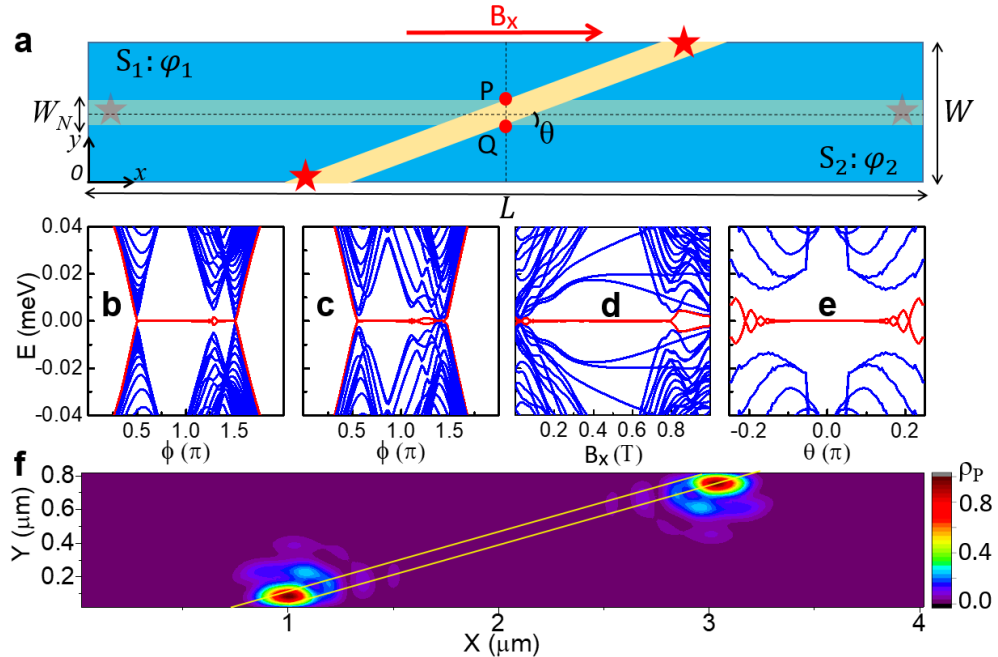
Supplementary Fig. 3 shows the spectrum evolution for the MBS fusion scheme in an SJ. The adiabatic evolution in the fusion scheme is verified by the calculated energy spectra evolution for the operations in nontrivial (A_1 - A_4) and trivial (B_1 - B_4) fusion. For any value of the continuously changing mini gates, the MBS are protected by the topological gap between the ground and first excited states which has the minimum value of $\sim 6 \mu\text{eV}$. The different signatures between the trivial and nontrivial fusions are verified by the calculated ρ_P and ρ_C of the fused MBS.



Supplementary Fig. 3. Calculated energy spectrum evolution for the operations in **a** nontrivial (A_1 - A_4) and **b** trivial (B_1 - B_4) fusion in an SJ, shown as a function of the relevant mini-gate voltage. Red and black lines: evolution of finite-energy states into MBS inside the topological gap. E and F indicate the two MBS pairs (degenerate ground states) in the $++-$ configuration (before fusion), while G and H indicate the ground and first excited state at $V_3 = -0.6 \mu\text{eV}$ in the $++++$ configuration (after fusion). **c-e** Sum of the probability densities, ρ_P , for E and F. **d-e** ρ_P for G and sum of the ρ_P for G and H. **f-h** The same as **c-e**, but shown for charge densities, ρ_C . The dashed line mark the N regions covered by the mini gates. The (minimum, maximum) values in **f**, **g** and **h** are (-0.07, 0.09), (-0.00009, 0.00004) and (-3.5, 2.9), respectively. The parameters are taken from Fig. 4 in the main text.

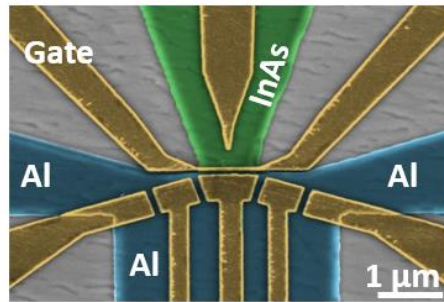
Supplementary Fig. 4: MBS robustness against the deviation of the magnetic field from the junction interface.

Supplementary Fig. 4 shows the robustness of the MBS against the misalignment angle, θ , between the N/S interface and the applied in-plane magnetic field. Our calculations reveal that topological superconductivity is supported for $\theta \leq 0.15\pi$.



Supplementary Fig. 4. **a** Schematic of a tilted junction with a misalignment angle θ from the applied B_x . MBS (stars) reside at the opposite ends of the N region (yellow). **b** Energy spectra for an SJ with $B_x = 0.4$ T as a function of the phase difference, $\phi = \varphi_1 - \varphi_2$. **c** Same as **b** but for a tilted junction with $\theta = 0.1\pi$. **d** Energy spectra for a tilted junction, $\phi = \pi$ and $\theta = 0.1\pi$ as a function of B_x . **e** Energy spectra for a tilted junction, $\phi = \pi$ and $B_x = 0.4$ T as a function of θ . **f** Probability density, ρ_P , for the lowest (red) energy states with $\phi = \pi$, $\theta = 0.1\pi$ and $B_x = 0.4$ T. When rotating the N region, we fix the P and Q points with the coordinates of $x_{P,Q} = L/2$ and $y_{P,Q} = (W \pm W_N)/2$. The geometric parameters are $L = 4$ μm , $W = 0.8$ μm and $W_N = 0.1$ μm . The other parameters are taken from Fig. 4 in the main text.

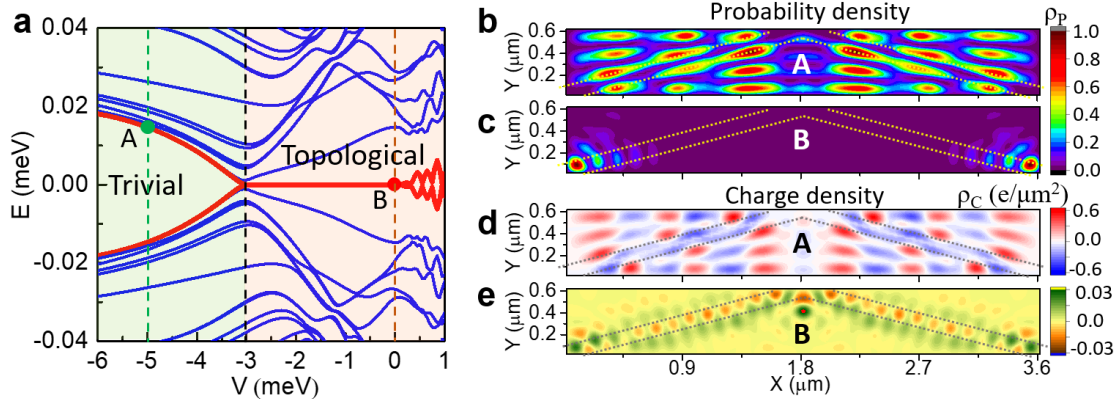
Supplementary Fig. 5: SEM image for the fabricated VJ with 5 mini-gates.



Supplementary Fig. 5. SEM image of a fabricated VJ with 5 mini-gates.

Supplementary Fig. 6: Gate-controlled topological transition in a VJ

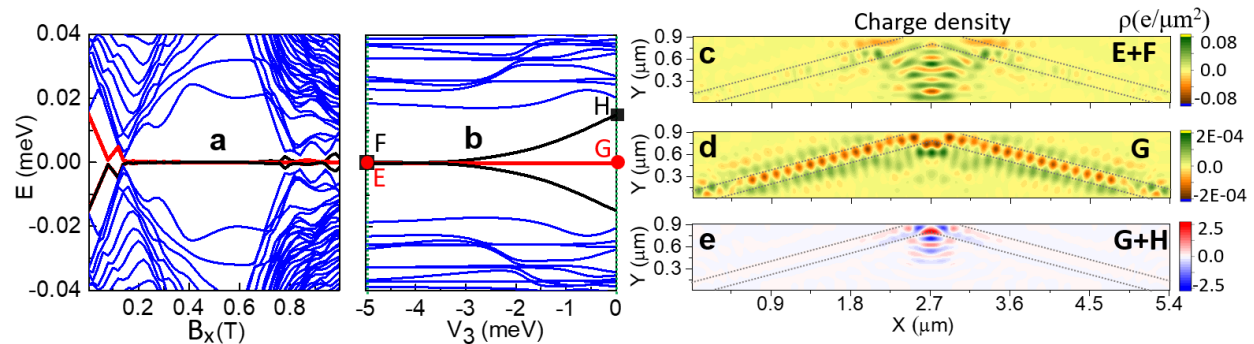
Supplementary Fig. 6 provides gate-controlled evolution of the energy spectra, ρ_P , and ρ_C for the trivial and topological states in the VJ. For topological states, the wave functions are localized at the ends of the N region, while the charge densities are vanishingly small and spread along the whole N region. For the trivial states, the wavefunctions are more delocalized, while the charge densities are much larger.



Supplementary Fig. 6. **a** The same as Fig. 6c in the main text, but with A (B) marking the lowest energy states at $V = -5$ (0) meV in the trivial (topological) region. **b** and **c** Probability density, ρ_P , normalized to its maximum value, for the lowest energy states (red lines) at $V = -5.0$ meV (marked as A) in the trivial region and $V = 0$ meV (marked as B) in the topological region, respectively. **d** and **e** The same as **b** and **c**, but for charge densities, ρ_C , respectively. The parameters are taken from Fig. 6 in the main text.

Supplementary Fig. 7: Energy spectrum and charge densities for a VJ with a larger size.

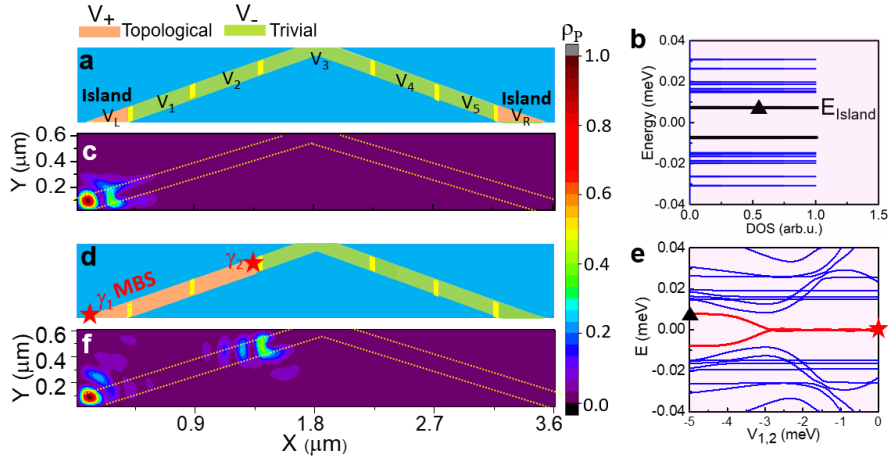
Supplementary Fig. 7 shows that the oscillations of the zero-energy modes can be reduced when the system size is increased. Correspondingly, ρ_C of the zero-energy modes decreases drastically.



Supplementary Fig. 7. **a** The same as Fig. 6f in the main text, but with $L = 5.4$ μm and $W = 0.9$ μm . **b** The same as the energy spectrum of A_3 in Fig. 7a in the main text, but with $L = 5.4$ μm and $W = 0.9$ μm . **c-e** The same as Figs. 7e-g in the main text, but with $L = 5.4$ μm and $W = 0.9$ μm . The (minimum, maximum) values in **c-e** are (-0.06, 0.08), (-0.00019, 0.00019) and (-2.2, 2.5), respectively. The dashed lines indicate the normal regions covered by the mini gates. The parameters are taken from Fig. 6 in the main text.

Supplementary Note 1: Preparation of the initial states through initializations

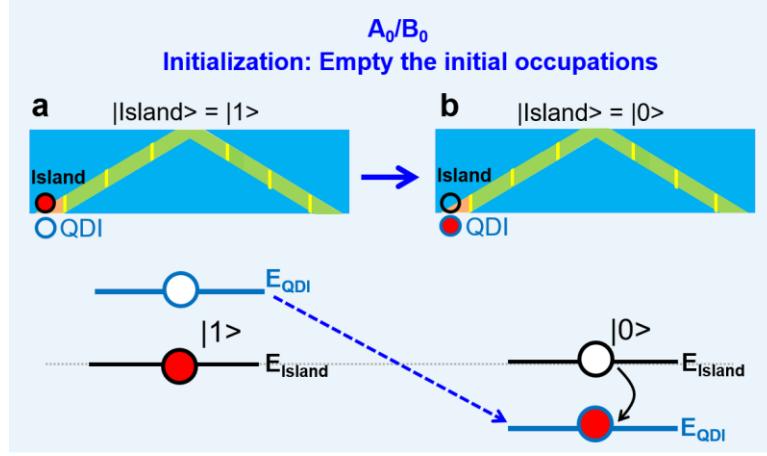
For a two-fermions system (f_{12} and f_{34}) discussed in the manuscript, there are four typical occupation states, depending on whether they are occupied ($|1\rangle$) or unoccupied ($|0\rangle$), i.e. $|00\rangle$, $|11\rangle$, $|10\rangle$, and $|01\rangle$. Based on the fusion rules given in Fig. 1 in the main text, irrespective of the initial state, the trivial fusion cannot change the fermion occupations, while the nontrivial fusion can always induce a superposition of the occupied and unoccupied states, having 50% probability to change the fermion occupations. As a result, we should observe charge fluctuations when repeating the nontrivial fusion, while no charge fluctuations when repeating the trivial fusion.



Supplementary Fig. 8. **a** Schematic of the VJ having five mini gates with voltages V_1 - V_5 and two additional half-length mini gates, with voltages V_L and V_R . We set $V_{L,R} = V_+ = 0$ (orange) and $V_{1-5} = V_- = -5$ meV (green) to engineer the two short mini-gates into the effective quantum islands. **b** Density of states for **a** with $V_L = V_+$ but $V_R = V_-$. **c** Probability density, ρ_P , of the E_{Island} marked by the triangle in **b**, supporting the formation of the quantum island. Schematic **d** and the spectrum evolution **e** when the topological region is extended by changing V_1 and V_2 from V_- to V_+ . **f** ρ_P of the lowest positive energy marked by the star in **e**, supporting the MBS formation. The parameters are taken from Fig. 6 in the main text.

However, if each time the initial state changes randomly, the trivial fusion may also give charge fluctuations (due to trivial change of the initial occupations), bringing possible false signature of the fusion rules. To overcome this problem, it is important to keep the same initial occupation in every fusion cycle. To prepare the initial occupations of f_{12} and f_{34} , we first need to generate two quantum islands to store the f_{12} and f_{34} . Such islands should form at the edge of the system to be accessible and flexibly controlled. Considering that our MBS are initially generated at the two VJ ends, we propose to create two quantum islands by adding half-length mini gates (L, and R), with voltages V_L and V_R at the ends of VJ, as shown in Supplementary Fig. 8a. Considering the length of the L (R) is small, when it is in the topological region, it can behave as an effective quantum island with the lowest energy level, E_{Island} , within the superconducting gap. Taking the quantum island L as an example, we calculate its energy spectrum and find the $E_{\text{Island}} \sim 8$ μ V as shown in Supplementary Fig. 8b. Our calculated probability density (Supplementary Fig. 8c) confirms the effective quantum island indeed forms at L. Such an island can store the fermion f_{12} . When the E_{Island} is occupied (unoccupied), the f_{12} is in $|1\rangle$ ($|0\rangle$) state. By changing the V_1 and V_2 from V_- to V_+ (Supplementary Fig. 8d), the topological region can be extended, and the f_{12} in quantum island adiabatically evolves into MBS ($f_{12} = \gamma_1 + i\gamma_2$), supported by the calculated spectrum evolution (Supplementary Fig. 8e). Since it is an adiabatic evolution, the f_{12} does not change its occupation until the nontrivial MBS fusion happens. Similarly, the fermion f_{34} can be stored at the quantum island R, and its occupation ($|1\rangle$ or $|0\rangle$) can be well defined

depending on whether its E_{Island} is occupied or not. Combing the occupations of f_{12} and f_{34} , we have four possible typical initial states ($|00\rangle$, $|11\rangle$, $|10\rangle$, and $|01\rangle$).



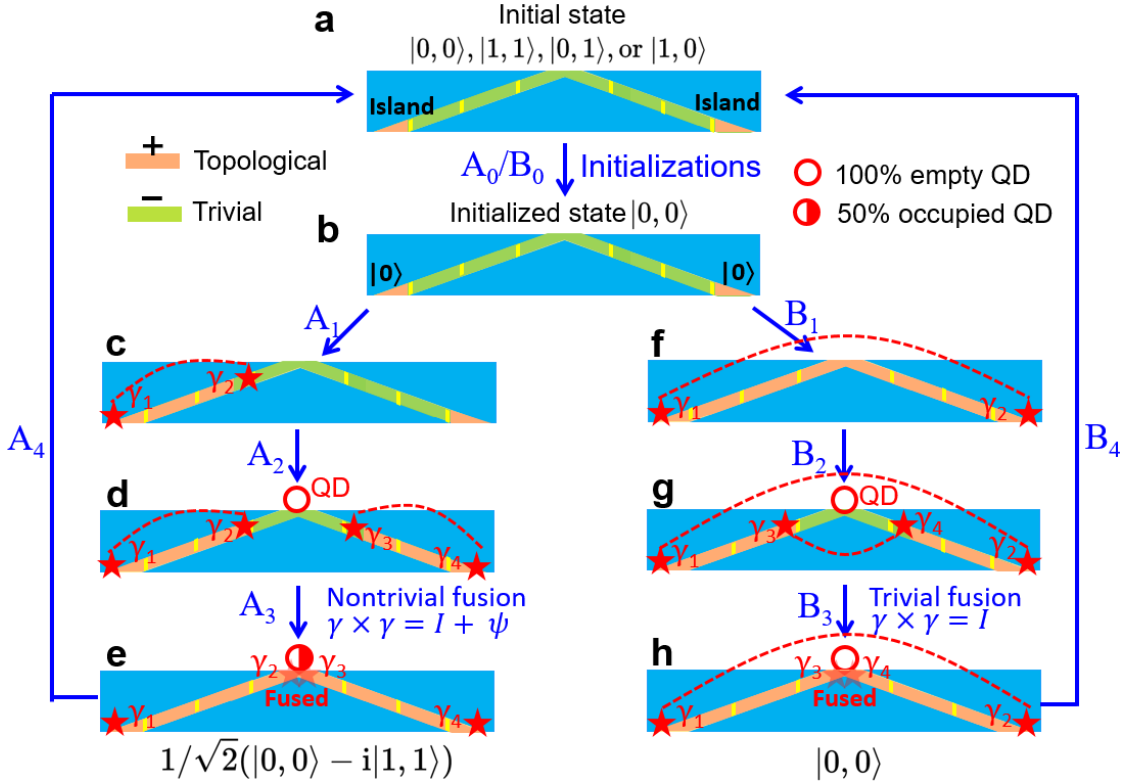
Supplementary Fig. 9. Schematic for the A_0/B_0 operation of “initialization”. **a** The initial occupation of the fermion $f_{12} = \gamma_1 + i\gamma_2$ in the quantum island. If the f_{12} is unoccupied ($|0\rangle$), it is our desired state and the initialization does not do anything. Thus, here we only show the case when f_{12} is occupied ($|1\rangle$), where the lowest positive energy level of the L quantum island ($E_{\text{island}} \sim 8\mu\text{eV}$ in Supplementary Fig. 8b) must be occupied. We couple the initializing QD, QDI (blue circle) with energy $E_{\text{QDI}} > E_{\text{island}}$, to the quantum island. **b** By shifting $E_{\text{QDI}} < E_{\text{island}}$, the charge of f_{12} in the quantum island can transfer into the QDI, leaving a $|0\rangle$ state for f_{12} . Similarly, the $|0\rangle$ state for f_{34} can be prepared by coupling another QD to the quantum island.

In principle, the initial state should be $|00\rangle$ because it is the ground state of the system. However, if for any reason the initial state is different (for example $|11\rangle$, $|10\rangle$, or $|01\rangle$ state), we can still empty it through additional QD by performing initialization procedure. Such initialization (A_0/B_0) shown in Supplementary Fig. 9 is added before the MBS generation and manipulation (A_{1-4}/B_{1-4}) in our fusion protocol (Supplementary Fig. 10), which can empty the initial occupations to give an initial state $|00\rangle$. We couple an additional initializing QD, QDI (Supplementary Fig. 9a), as a reservoir to receive the occupied fermion in the L quantum island and drive f_{12} into the $|0\rangle$ state. An advantage of using the QDI is that we can flexibly control its energy and coupling with the quantum island by gating [5]. Now, let us see how the QDI helps to empty the quantum island. For the $|0\rangle$ state, it is our desired state and the initialization operation does nothing. For the $|1\rangle$ state, by initially making the highest unoccupied energy level of the QDI, $E_{\text{QDI}} > E_{\text{island}}$ (Supplementary Fig. 9a), and then making the $E_{\text{QDI}} < E_{\text{island}}$ (Supplementary Fig. 9b), the charge of f_{12} in the L island can transfer into the QDI, leaving a $|0\rangle$ state for f_{12} . Similarly, we can drive f_{34} into the $|0\rangle$ state. After such an initialization, f_{12} and f_{34} are in the desired $|00\rangle$ state. Then we decouple the QDI with the VJ to make sure the QDI does not perturb the MBS manipulations in the VJ.

Supplementary Note 2: Protocol and spectrum evolution for the MBS fusion in a VJ

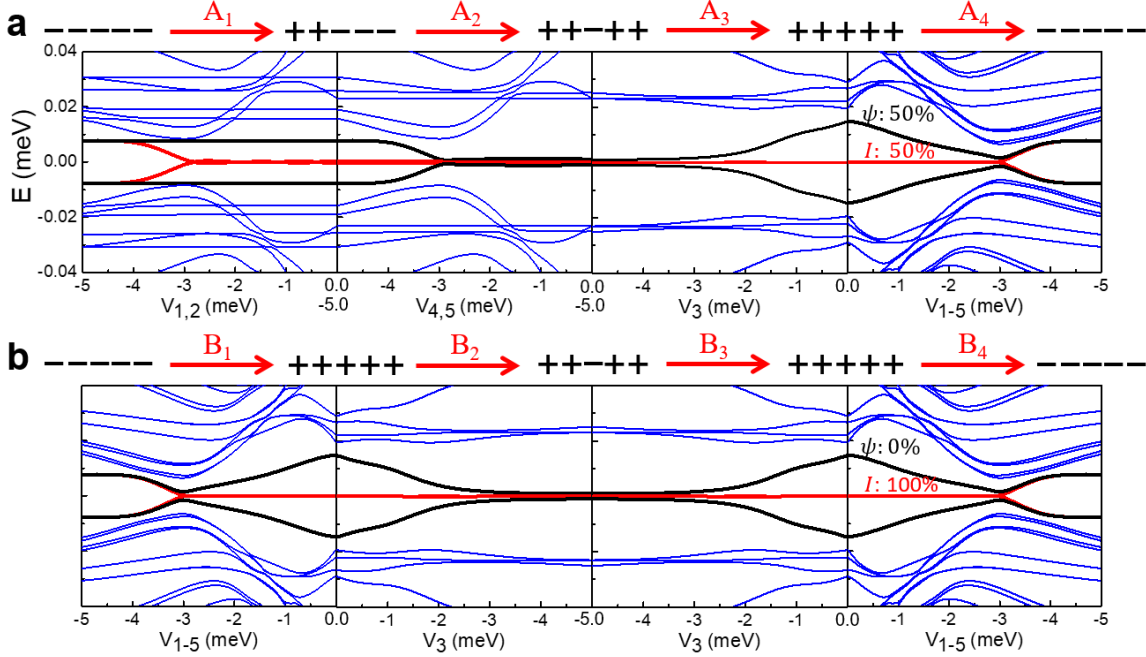
With the initialization, the initial VJ state is prepared as $|00\rangle$. Then we can perform A_1 - A_4 (B_1 - B_4) operations to implement the MBS nontrivial (trivial) fusion as shown in Supplementary Fig. 10. The spectrum evolution of A_1 - A_4 and B_1 - B_4 is shown in Supplementary Fig. 11. We can see two quantum island states can adiabatically evolve into two MBS pairs, where their pair configurations depend on the A_{1-2}/B_{1-2} operations. The operation A_3 fuses the MBS from different pairs and gives a nontrivial fusion, accessing both vacuum, I , and an unpaired fermion, ψ , with 50% probability, while the B_3 trivially fuses the MBS from the same pairs, corresponding to I with 100% probability. After A_3/B_3 , we use the QPC to detect the QD charge

number, Q_{QD} . For the trivial fusion, the Q_{QD} is 0; while for the nontrivial fusion, the Q_{QD} is 0 or 1e with the same probability, giving an expectation value of 0.5e. Such a different fusion outcome is supported by our dynamical simulations in Supplementary Fig. 12. After the QPC charge sensing detection, we perform A_4/B_4 operations to reset the system. By repeating such A_0-A_4 (B_0-B_4) operations, we can repeat the MBS fusion with the same $|00\rangle$ occupation, where every time the fusion occurs (the system goes to + + + + after A_3/B_3), we use the QPC to detect the Q_{QD} . The detected current, I_{QPC} , through the QPC is denoted by I_{TF} (I_{NF}) for the trivial (nontrivial) fusion. While the expected I_{TF} remains the same, the I_{NF} fluctuates during the fusion cycles. To suppress the possible trivial background charge fluctuation, we can focus on the difference, ΔI_{F} , between I_{TF} and I_{NF} . Measuring such a fluctuating ΔI_{F} is a direct evidence for the non-Abelian statistics of MBS.



Supplementary Fig. 10. Probing non-Abelian statistics through MBS fusion in a VJ coupled with a detection QD. The scheme is supported by the calculated probability and charge densities in Fig. 7 in the main text, spectrum evolution in Supplementary Fig. 11, as well as the dynamical simulations in Supplementary Fig. 12. The stars indicate MBS, and the dashed lines link the same MBS pair. **a** Initial trivial state with four typical occupations ($|00\rangle$, $|11\rangle$, $|01\rangle$, or $|10\rangle$) in —— mini gates with two quantum islands. **b** A_0/B_0 : Initialization as shown in Supplementary Fig. 9, where the initial state $|00\rangle$ is prepared. **c** A_1 : changing —— to + + —, MBS pair (γ_1, γ_2) is created. **d** A_2 : changing + + — to + + + +, a second MBS pair (γ_3, γ_4) is created. Then coupling a QD at the apex and making the QD empty. **e** A_3 : changing + + + + to + + + + +, the MBS (γ_2, γ_3) are nontrivially fused at the apex. As a result, the occupation changes into the superposition of $|00\rangle$ and $|11\rangle$, accessing both vacuum, I , and an unpaired fermion, ψ , with 50% probability. After A_3 , the QPC shown in Fig. 6 in the main text is used to detect the QD charge number, with the expected same probability for charge zero and one. **f** B_1 : changing —— to + + + + +, the MBS pair (γ_1, γ_2) is created. **g** B_2 : changing + + + + + to + + + + +, a second MBS pair (γ_3, γ_4) is created. Then coupling the QD at the apex and making the QD empty. **h** B_3 : changing + + + + + to + + + + + +, the MBS (γ_3, γ_4) are trivially fused and the occupation is the same as the initial $|00\rangle$, corresponding to I with 100% probability. After B_3 , the QPC is used to detect the QD charge number and zero charge is expected. **A₄/B₄**: Resetting the system: changing + + + + + to ——, and

decoupling the VJ with the QD. As a result, the system returns to the initial two quantum island states. MBS fusion can be repeated following such operations.



Supplementary Fig. 11. Calculated energy spectrum evolution for the operations of **a** nontrivial (A₁-A₄) and **b** trivial (B₁-B₄) fusion for a VJ in Supplementary Fig. 10, shown as a function of the relevant mini-gate voltage. Red and black lines: evolution of finite-energy states into MBS inside the topological gap.

Supplementary Note 3: Dynamical simulations for the MBS fusion in a VJ

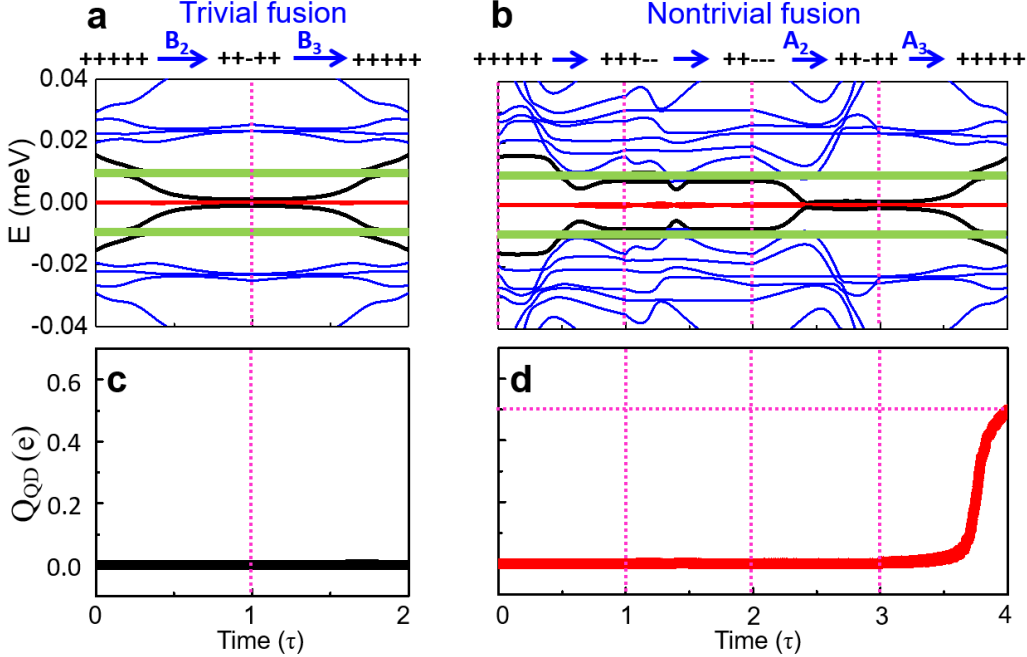
With the QD coupled to the VJ, the Hamiltonian for the system is $H = H_{VJ} + H_{QD} + H_{V-Q}$. Here, the H_{VJ} [given by Eq. (2) in the main text] describes the VJ. For simplicity, we suppress the spin index in the following terms. $H_{QD} = E_{QD} d^\dagger d$ describes the QD with a gate-tunable energy level E_{QD} , where d^+ (d) creates (annihilates) an electron in the QD. $H_{V-Q} = \sum_{i \in \text{apex}} (\lambda c_i^\dagger d + H.C)$ describes the coupling between the QD and VJ apex, where c_i^\dagger creates an electron in the VJ and λ is the coupling strength. To elucidate the fusion outcomes and reveal how they can be detected by the QD charge sensing, we perform dynamical simulations based on the time-dependent Bogoliubov–de Gennes equation [6, 7]

$$i\hbar \frac{\partial}{\partial t} \psi(t) = H(t) \psi(t),$$

where $\psi(t)$ is the quasiparticle wave function in the Nambu representation. The evaluation of the wave function during a time Δt is given by $\psi(t + \Delta t) = U(t + \Delta t, t) \psi(t)$ with the time-evolution operator

$$U(t + \Delta t, t) = \tau \exp \left[-i \int_t^{t+\Delta t} d\xi H(\xi) \right],$$

where τ is the switching time to control the evolution speed. For a sufficiently short Δt , the time-evolution operator is approximated as $U(t + \Delta t, t) \approx \exp[-iH(t)\Delta t]$.



Supplementary Fig. 12. **a-b** Calculated spectrum evolution and **c-d** corresponding charge average of the QD, Q_{QD} , during the nontrivial and trivial fusion processes with a cyclic loop. The green lines in **a** and **b** indicate the energy levels of the QD. The parameters of $E_{QD} = 10 \mu\text{eV}$, $\lambda = 3 \mu\text{eV}$, and $\tau = 2.4 \text{ ns}$ are used for dynamical simulations. Other parameters are taken from Fig. 7 in the main text.

We show how the QD affects the spectrum evolution during the fusion in Supplementary Figs. S12 a and b. To estimate the QD charge change after trivial and non-trivial fusions, we perform a time evolution for the initial state $|00\rangle$, corresponding to all negative (positive) states being occupied (empty). Details about the preparation of the $|00\rangle$ state are discussed in Supplementary Note 1. For adiabatic processes and low energy excitations, only the four states with energies $\{-E_2, -E_1, E_1, E_2\}$ (ordered from smaller to larger) closer to zero are involved in the fusion process. During the trivial fusion, the occupancy of these states remain unchanged. However, during the non-trivial fusion the occupancy of the two negative energy states is transferred, with 50% probability to the positive energy states. In our scheme, the QD level is set to the final value of E_2 , allowing to detect the final charge transferred into this, initially empty, energy state. Since both E_1 and E_2 are initially empty and the occupancy transfer from level $-E_2$ to E_2 is forbidden by particle-hole symmetry, the final charge measured in the QD can only originate from the initially occupied state ψ_{-E_1} . The average charge in the QD can be estimated as $Q_{QD} = e \times P_{-E_1 \rightarrow E_2} \times P_{E_2 \rightarrow QD}$, where $P_{-E_1 \rightarrow E_2}$ is the probability for the occupancy of level $-E_1$ to be transferred to E_2 and $P_{E_2 \rightarrow QD}$ is the probability that the charge in level E_2 tunnels into the QD. If the process is adiabatic, the outcome of trivial and non-trivial fusions are, $P_{-E_1 \rightarrow E_2} \rightarrow 0$ and $P_{-E_1 \rightarrow E_2} \rightarrow \frac{1}{2}$, respectively. The time-dependence of the QD charge can therefore be estimated as $Q_{QD}(t) = e \times |\langle \psi_M(t) | \psi_{QD} \rangle|^2$, where $\psi_M(t)$ describes the time evolution of the energy level $-E_1$ [i.e., $\psi(0) = \psi_{-E_1}$] and ψ_{QD} is the wavefunction of the QD.

For the trivial fusion, the MBS $\psi_M(\gamma_1, \gamma_2)$ is first created in the $++++$ configuration. Taking it as an initial state, we perform dynamical simulations following the sequence of B_2 [creating (γ_3, γ_4)] and B_3 [fusing (γ_3, γ_4)] as shown in the fusion protocol (Supplementary Fig. 10). The calculated Q_{QD} remains zero (Supplementary Fig. 12c), indicating the 100% fusion channel I in the trivial fusion. For the nontrivial fusion, (γ_1, γ_2) is created in the $+ + - -$ configuration. To clearly see the difference between the trivial and nontrivial fusion, it is important to perform the dynamical simulations from the same initial state in both

cases. To achieve this, starting from the same initial ψ_M as that in the trivial fusion, we first adiabatically move (γ_1, γ_2) from $+++++$ to $++---$ configuration and then follow the sequence of A_2 [creating (γ_3, γ_4)] and A_3 [fusing (γ_2, γ_3)] to finish the nontrivial fusion process as shown in Supplementary Fig. 12b. In contrast to the trivial fusion, the calculated Q_{QD} is rising up after the nontrivial fusion occurs (Supplementary Fig. 12d), indicating there is a finite probability that the QD receives an unpaired fermion from the VJ. Furthermore, the maximum $Q_{QD} = 0.5e$ is consistent with the expected equal probabilities of channels I and ψ in the nontrivial fusion. Such different fusion outcomes from the dynamical simulations clearly demonstrate the non-Abelian statistics of the MBS fusion.

- [1] Alicea, J. New directions in the pursuit of Majorana fermions in solid state systems, *Rep. Prog. Phys.* **75**, 076501 (2012).
- [2] Scharf, B. & Žutić, I. Probing Majorana-like states in quantum dots and quantum rings, *Phys. Rev. B* **91**, 144505 (2015).
- [3] Pientka, F. et al. Topological superconductivity in a planar Josephson junction. *Phys. Rev. X* **7**, 021032 (2017).
- [4] Hell, M., Leijnse, M. & Flensberg, K. Two-dimensional platform for networks of Majorana bound states. *Phys. Rev. Lett.* **118**, 107701 (2017).
- [5] Hanson, R., Kouwenhoven, L. P., Petta, J. R., Tarucha, S. & Vandersypen, L. M. Spins in few-electron quantum dots. *Rev. Mod. Phys.* **79**, 1217-1265 (2007).
- [6] Amorim, C. S., Ebihara, K., Yamakage, A., Tanaka, Y. & Sato, M. Majorana braiding dynamics in nanowires. *Phys. Rev. B* **91**, 174305 (2015).
- [7] Sanno, T., Miyazaki, S., Mizushima, T. & Fujimoto, S. Ab initio simulation of non-Abelian braiding statistics in topological superconductors. *Phys. Rev. B* **103**, 054504 (2021).